

Rainfall microphysical characterization over the Mediterranean area during the GPM era

17

Leo Pio D'Adderio¹, Federico Porcù², Giulia Panegrossi¹, Ali Tokay³,
Gianfranco Vulpiani⁴, Stefano Dietrich¹

*National Research Council of Italy, Institute of Atmospheric Sciences and Climate (CNR-ISAC),
Rome, Italy¹ Department of Physics and Astronomy "Augusto Righi," University of Bologna,
Bologna, Italy² Joint Center for Earth Systems Technology, University of Maryland Baltimore
County NASA Goddard Space Flight Center, Greenbelt, MD, United States³ Department of Civil
Protection, Technical-Scientific Activities Office for Risk Prediction and Prevention, Rome, Italy⁴*

CHAPTER OUTLINE

17.1 Introduction	2
17.2 Data and instrumentation	5
17.2.1 DPR overview and products	6
17.2.2 Ground-based radar network	6
17.2.3 Two-dimensional video disdrometer	7
17.3 Preliminary analysis: single- versus dual-frequency DPR comparison	8
17.3.1 Data selection	8
17.3.2 DF- and SF-based DPR standard outputs comparison	10
17.4 DF- and SF-based rain and DSD parameters comparison at NSL	13
17.5 Validation of microphysical and integral DSD parameters	27
17.5.1 Microphysical and integral DSD parameters estimation from GR data	29
17.5.2 The neural network approach	29
17.5.3 The empirical relationships approach	30
17.5.4 A preliminary analysis on the derivation of the DSD parameters	31
17.5.5 DPR and DPR-GMI performance	33
17.5.6 Sensitivity analysis	44
17.6 Conclusion	48
References	52
Further reading	56

17.1 INTRODUCTION

The Mediterranean basin is recognized as a climatic hotspot, often affected by severe weather events that are becoming more and more frequent in the last decades (Giorgi, 2006). Extreme events originating over the Mediterranean Sea and hitting the coast can have tremendous impact from hydrological point of view as well as in terms of human and economic losses. A correct characterization of the precipitation occurring over the Mediterranean area becomes fundamental to improve the knowledge of these systems. Spaceborne passive microwave (PMW) radiometry is recognized as the most suitable tool for global precipitation monitoring and quantification. At the same time the active microwave radiometry (AMW, i.e., the weather radars) gives a more detailed and resolute description of a precipitating system allowing to reconstruct the tridimensional structure of it.

The Global Precipitation Measurement (GPM) Core Observatory (CO) combines these two aspects carrying the two most advanced spaceborne sensors dedicated to global precipitation monitoring: the GPM microwave imager (GMI) radiometer and, for the first time, a dual-frequency precipitation radar (DPR), at the Ka-band and Ku-band. In fact, one of the goals of the GPM, a joint mission between the National Aeronautics and Space Administration (NASA) and the Japan Aerospace Exploration Agency (JAXA), is to demonstrate that a radar–radiometer space-based measuring system can provide frequent and accurate precipitation measurements at global scale. The DPR provides insights into the 3-D structure and properties of precipitating clouds and is currently considered the main calibration instrument for radiometer-derived global precipitation estimates. An important goal of the GPM mission is to harmonize the products obtained from the heterogeneous constellation of microwave radiometers, provided by international satellite agencies, to converge toward uniform global precipitation products (Hou et al., 2014; Panegrossi et al., 2016; Skofronick-Jackson et al., 2017). The GPM mission provides precipitation estimates at different temporal scales: from 3-D instantaneous precipitation structure to hourly/daily/monthly rain rate at the ground, covering the globe between 65°S and 65°N (Hou et al., 2014). The retrieval of the 3-D structure of the precipitation is possible thanks to the development of the dual-frequency (DF) retrieval algorithm that provides the particle size distribution (PSD) parameters (hereafter, we will refer to the DSD—drop size distribution—since we focused on the analysis of liquid precipitation only): the mean mass-weighted diameter (D_m) and the normalized intercept parameter (N_w), as well as different DSD integral parameters, such as precipitation rate, liquid, and ice water contents (Hamada & Takayabu, 2016). At the same time, single-frequency (SF) retrieval algorithm–based products (Ka- and Ku-only) also provide DSD parameters (i.e., D_m and N_w) as standard output but additional constraints have been set to reach this end. On the other hand, the combined product DPR–GMI exploiting the DPR measurements along with multifrequency brightness temperature measurements from the GMI is able to provide the DSD parameters as well (Grecu et al., 2016).

Since the launch of the GPM-CO in February 2014, the number of studies dedicated to the validation of the GPM products has increased due also to the availability of reference datasets around the globe and to dedicated field experiments (Schwaller & Robert Morris, 2011). These studies take the DSD and rain integral parameters, estimated or measured mainly by radar and rain gauge networks as a ground reference. In this framework, within the GPM ground validation (GV) activity, two postlaunch field campaigns were carried out: the Integrated Precipitation and Hydrology Experiment (IPHEX) (D'Adderio et al., 2015) and the Olympic Mountains Experiment (OLYMPEX) (Houze et al., 2017). The data collected during the field campaigns represent a benchmark both for a direct comparison with GPM-CO overpasses and for testing the reliability of ground measurements as a reference to validate GPM products (Chandrasekar et al., 2015; Chen & Chandrasekar, 2017). In fact, one of the main objectives of GPM GV is the quantification of the uncertainties in the DSD and precipitation retrievals through comparative studies with the ground-based estimates. DPR measurements are affected by several sources of error, including the effects of attenuation, especially at Ka-band (Meneghini et al., 2015); ground clutter (Kubota et al., 2016), which interferes with near-surface rain observations; nonuniform beam filling (NUBF), which is related to the variability of precipitation within the DPR footprint (Tokay et al., 2017); and multiple scattering (Battaglia et al., 2014). Although the DPR and DPR-GMI algorithms attempt to correct for most of these effects, the effectiveness of the correction and the accuracy of the retrievals, in general, must be evaluated by direct comparisons to ground-based data. Consequently, the quantification of the error in estimating the surface rainfall intensity (R) and DSD parameters at different locations and seasons is a key point to evaluate the performance of the GPM products.

Speirs et al. (2017) analyzed the agreement between the DPR and the ground radar (GR) (solid and liquid) precipitation estimates over Switzerland, taking advantage of the terrain complexity to evaluate the impact of the orography. They analyzed both SF- (Ka- and Ku-only) and DF-based products. Petracca et al. (2018) performed the similar analysis over Italy, assessing DPR precipitation product accuracy as a function of season, rain intensity, and GR quality. They both found a general underestimation of the precipitation that can be significant for heavy rain or in presence of complex terrain. In both papers the authors used the version-4 (V04) of the DPR algorithms. Watters et al. (2018) compared the DPR and combined DPR-GMI version-5 (V05) rainfall rate estimates with Great Britain and Ireland radar composite product. Considering a finer and a coarser horizontal spatial resolution, they found a general underestimation of rain intensity by both DPR and DPR-GMI products. Direct validation of the DSD parameters is made more difficult by the intrinsic impossibility to have ground-based measurements of DSD at scales comparable to DPR footprints and to have a statistically significant dataset. Seto et al. (2016) analyzed the global variability of DPR-based D_m estimates as a function of the surface type and latitude. They found that D_m is larger over land than over ocean, where the difference between intertropical and midlatitude zones is more marked. More recently, D'Adderio et al. (2018) investigated the quality of

both SF- and DF-based (and of combined DPR–GMI) D_m estimates over the central Mediterranean region through a comparative study with GR D_m estimates. The results show a better agreement with GR estimates for stratiform than convective precipitation, while the combined DPR–GMI product outperforms all DPR products. A negligible difference is found between the results over land and over sea. Very similar results were found by Gatlin et al. (2020) which validated the GPM-based DSD parameters through a comparison with estimations from GRs of GPM validation network (VN). In other studies, DPR products are used to characterize precipitation structure. Iguchi et al. (2018) focused on intense ice precipitation as detected by the new flag released in the V05 of DPR products both comparing it with ground measurement reference and evaluating its distribution at global scale analyzing one year of data. Among the other case studies analyzed in their work, they show an effective application of this new flag to an exceptionally severe hailstorm that occurred in 2015 in the Mediterranean area and deeply analyzed by Marra et al. (2017). The available literature evidence that both SF- and DF-based DPR products are used in validation studies without any prior analysis about the agreement between the two outputs. These products are used either to characterize the microphysics structure of the precipitation or to analyze the properties and the evolution of a precipitation system or to evaluate the quality of the precipitation estimation at the ground. The DPR takes advantage of the DF to mitigate the error in converting the reflectivity to precipitation rate thanks to the estimation of the DSD parameters [not possible with an SF radar unless to apply to the SF algorithm the DSD dataset created by DF algorithm (Iguchi et al., 2018)].

Starting from this consideration, an intercomparison between the SF- and the DF-based DPR products during rain events could highlight similarities and differences between the two groups of products. The Mediterranean, for the reasons evidenced above, represents an interesting area where to perform this type of analysis. In addition, the liquid precipitation in the Mediterranean area presents midlatitude characteristics, making the results of this analysis to be generally applicable to midlatitudes. D’Adderio et al. (2018) analyzed the D_m – Z_{DR} (differential reflectivity) relationship at different sites, showing that the relationship between DSD parameters over the Mediterranean [i.e., data collected during hydrological cycle in the Mediterranean EXperiment (HyMeX) field campaign] does not differ from the other ones for midlatitude sites over the United States. Caracciolo et al. (2008) analyzing a disdrometric dataset collected over northern Italy found that the Z – R relationship is very similar to the Z – R relationships derived at midlatitudes. Finally, the GPM products are more and more used to characterize and describe different precipitation systems (Mroz et al., 2017; Ni et al., 2017; Panegrossi et al., 2016). At the same time, PMW and AMW sensors onboard of GPM constellation are able both to monitor the evolution and to provide the 3-D description of heavy precipitation systems. Among the others and very recently, Panegrossi et al. (2020) described three different precipitation systems from different points of view ranging from quantitative estimation of precipitation amount to the microphysical characterization of them; Marra et al. (2019) exploited the unprecedented data provided by

the GPM mission to investigate tropical-like cyclone, the so-called Medicane (MEDiterranean hurriCANE).

In this frame, this chapter focuses on two different analyses linked to each other: if, on one side, we investigate the differences between SF- and DF-based DPR products, on the other side, we investigate the reliability of both DPR and DPR–GMI algorithms in estimating microphysical and integral DSD parameters (namely, D_m , N_w , and RR) also trying to identify conditions that affect the goodness of the estimation. While for the first part of the study we use 5 years of DPR data (i.e., from 2015 to 2019), for the second part, we considered a number of DPR overpasses, in the same period, over Italy where coincident measurements with GR network were available.

17.2 DATA AND INSTRUMENTATION

To perform the analysis a large set of data have been used: 5 years of GPM (both DPR and combined DPR–GMI) data, from January 2014 to December 2019. The analysis focused only on liquid precipitation to avoid the issues related to snowfall retrieval in DPR products (Casella et al., 2017). Totally, more than 685,000 DPR footprints have been selected. The target area, covering the Italian Peninsula, is limited between 36–48°N and 5–20°E to ensure enough number of samples over land and over sea. As ancillary information, the data collected by the 2-D video disdrometer (2DVD) (Kruger & Krajewski, 2002) during four field campaigns of the GPM GV and two permanent sites across the United States have been also used. These data are part of the GPM GV program consisting of a number of prelaunch and post-launch field campaigns in the GPM era (D’Adderio et al., 2015; Tanelli et al., 2017), as well as of a permanent measurement site (e.g., Wallops Island, Virginia and Huntsville, Alabama). Since we limited our analysis to the liquid precipitation only, the GPM GV field campaigns, which were more focused on the characterization of solid precipitation, were not considered in this study. The disdrometer data used in this study have been mainly collected during spring-early/summer (only OLYMPEx field campaign has been carried out in the fall-early winter season). Moreover, 2DVD data in the Mediterranean region collected during the HyMeX (Somot et al., 2014) field campaign (late summer-early fall season) have also been used. Totally, more than 185,000 1-min 2DVD measurements were analyzed by combining all the data available. Although different disdrometers (i.e., 2DVD, Parsivel², etc.) operated through the field campaigns considered, their performances in measuring the DSD are very similar (Tokay et al., 2017). To validate the GPM measurements, the data collected by the Italian GR network have been considered. Specifically, 42 GPM overpasses over Italy, collected mainly from spring to fall seasons (from April to the beginning of November) in the 2015–19 time interval, have been analyzed.

17.2.1 DPR OVERVIEW AND PRODUCTS

The DPR is the first DF spaceborne radar operating at both Ka- (35 GHz) and Ku-band (13.6 GHz). The DPR employs three scanning modes: matched scan (Ms), normal scan (NS), and high-sensitivity scan (HS). The Ka- and Ku-band radar Ms footprints of the inner swath consist of 25 angle bins with range sampling at 125 m while the Ku-band radar (NS) covers the full swath with 49 angle bins (numbered from 1 to 49) with a range sampling of 125 m both covering 22 km of atmosphere with 176 vertical bins. The HS Ka-band radar footprints are interlaced with matched Ku-/Ka-band footprints and consist of 24 angle bins with range sampling at 250 m. The swath widths of Ka- and Ku-band radars are 120 and 245 km, respectively, while both Ka- and Ku-band footprints at nadir are approximately 5 km in diameter. For this work the V06 level-2 products from both DPR (2A-DPR) and DPR-GMI (2B-CMB) algorithm have been used. The 2A-DPR products provide three scan types: 2A-DPR NS, 2A-DPR HS, and 2A-DPR Ms. The 2A-DPR HS output parameters are derived from Ka-only HS measurements (even though some ancillary DF information may be used). The inner swath (i.e., footprints 13–37) of 2A-DPR NS as well as the 2A-DPR Ms (hereafter DPR Ms) are processed by using the combined information from both the frequencies, while the output parameters of the outer swath (footprints 1–12 and 38–49) of 2A-DPR NS are derived from Ku-only measurements (Iguchi et al., 2017). On the other hand, the 2A-Ku NS products (hereafter DPR NS) are derived only from Ku measurements (the products of the outer swath of 2A-DPR NS and 2A-Ku NS are identical) over the full swath. Consequently, in the following analysis, the so-called DPR NS refers to the 2A-Ku NS products to test the performance of the whole swath using only the Ku-band data. The D_m , N_w , and RR , which are the three DSD parameters analyzed in this study, are a standard output of all three DPR scan types. On the other hand, the 2B-CMB level products combine the information from the active sensor DPR and passive sensor GMI and provide two scan types: 2B-CMB NS and 2B-CMB Ms. As for the DPR algorithm, The DPR-GMI algorithm provides D_m , N_w , and R as standard output, by using the SF- and DF information for 2B-CMB NS and 2B-CMB Ms, respectively. The precipitation has been divided into stratiform, convective, and other (for those cases which are classified as neither stratiform nor convective) according to the DPR classification. The classification is based on analysis of the vertical profile of the measured DF ratio when the DF data are available; otherwise, it is based on the presence of the bright band (BB) together with a horizontal (H) or vertical (V) method (Iguchi et al., 2017).

17.2.2 GROUND-BASED RADAR NETWORK

The Italian GR network includes 20 C-band and 3 X-band radar, managed by 11 administrations. Moreover, 7 out of 20 C-band and the 3 X-band systems (all with dual-polarization capability) are directly managed by the Department of Civil Pro-

tection (DPC), which is also the developer and distributor of the national precipitation product. The processing architecture is basically composed of two main steps, where the radar measurements are first locally processed by a unique software system, and then all the products are centralized to generate the national-level products. For the present work, three C-band radars located in the center of Italy at Il Monte (41.9402°N, 14.6209°E), Serano (42.8667°N, 12.8003°E), and Armidda (39.8822°N, 9.4937°E), and two C-band radars located in the south Italy at Lauro (37.1131°N, 14.8356°E) and Pettinascura (39.3698°N, 16.6183°E), at the altitudes of 700, 1500, 1286, 980, and 1725 m.a.s.l., respectively, have been used. Of the 42 case studies considered, only one case and two cases have been recorded by the Pettinascura and Lauro GR, respectively, while several cases have been simultaneously observed by two or three radars. The scan strategy for the operational DPC GR involves eleven plane position indicator inverse scans at inclination angles ranging between 16 degrees and 90 degrees, depending on the starting time of the scan, and 0.5-degree width uneven angle bin steps. The data have a time resolution of 5 min, while the 1-degree beamwidth and the 150-m range size ensure a quite good spatial resolution. The data processing begins with the identification and compensation for nonweather returns based on the use of the fuzzy logic approach proposed in Vulpiani et al. (2012). The partial beam blockage is evaluated as proposed by Bech et al. (2003) and compensated up to 70% (Tabary, 2007). The differential phase Φ_{DP} is processed through the iterative finite difference scheme proposed in Vulpiani et al. (2012, 2015) using a 3-km size moving window. The resulting Φ_{DP} , which is immune to any potential system offset and unfolding, is used to correct for rain path attenuation (Bringi et al., 1990), whereas specific differential phase K_{DP} is used jointly with reflectivity factor Z and differential reflectivity Z_{DR} to estimate the DSD parameters, as described in Section 17.5.2. Given the topography of the region (all the radars are located at significant altitudes since they are surrounded by mountains), the lowest beam map (LBM) reflectivity of the GR has been spatiotemporally matched with the DPR measurements. The spatiotemporal matching was considered valid only when the DPR identified the phase of precipitation as liquid at near-surface level (NSL).

17.2.3 TWO-DIMENSIONAL VIDEO DISDROMETER

The data used in this study include the latest version of the 2DVD (Kruger & Krajewski, 2002) disdrometer, which has been deployed during GPM GV field campaigns and at permanent sites both before and after the GPM launch. This instrument is considered among the new standards for disdrometric measurements. The 2DVD measures size, fall velocity, and shape of each hydrometeor falling within its measurement volume so that the DSD (more in general the PSD because of its capabilities in recording both solid and liquid hydrometeors) is available with a temporal resolution of 1 min (with the possibility to change the time resolution as a function of the user needs). It is equipped with two high-speed line scan cameras (A and B) with orthogonal projections. The matching images from camera A and

camera B are critical to obtain geometrical properties of the hydrometeor correctly. The hydrometeor size is estimated by counting the number of pixels occupied in each image in both cameras, while the fall velocity of hydrometeors is directly related to the elapsed time between the two planes. In the presence of rain the deviation of measured fall speed from Gunn and Kinzer (1949) observations may hint at a calibration error or oscillatory behavior, as documented in Thurai et al. (2013). The secondary drops either due to the splashing or dripping at the edge of sampling cross section or mismatching are filtered out using a threshold where the measured fall speed is faster or slower than plus or minus 50% of the Gunn and Kinzer (1949) observations. To the end of this study, the 0- to 10-mm range of raindrop diameters has been divided in 50 bins 0.2-mm width. The data collected by the 2DVD during the rain events from four different midlatitude GPM GV field campaigns that are used in this study include Iowa Flood Studies (IFloodS; 41.68°N, 91.58°W), Midlatitude Continental Convective Clouds Experiment (MC3E; 36.78°N, 97.18°W), IPHEX (35.58°N, 82.58°W; D'Adderio et al., 2015), and the OLYMPEx (47.58°N, 123.58°W; Houze et al., 2017). In addition, the data collected at permanent sites of Wallops Island, Virginia (Wallops; 37.98°N, 75.58°W) and Huntsville, Alabama (Alabama; 34.78°N, 86.68°W) have been also used as well as the data collected in Italy during the HyMeX (41.98°N, 12.58°E) (Drobinski et al., 2014). The disdrometer data have been used for multiple purposes ranging from the derivation of a relationship to estimate D_m and N_w to the simulation of the radar variables.

17.3 PRELIMINARY ANALYSIS: SINGLE- VERSUS DUAL-FREQUENCY DPR COMPARISON

17.3.1 DATA SELECTION

As reported in Section 17.1, the first part of this chapter is dedicated to the inter-comparison between the DF- and SF-based DPR products to highlight both similarities and differences between the two categories of products. To this end the version-6 (V06) Level-2 DPR products have been used. In particular, the DF-based 2ADPR-Ms product, and the SF-based 2AKa-Ms (Ka-band only) and 2AKu-NS (Ku-band only) products have been considered [please refer to GPM File Spec NASA/JAXA (2020); Iguchi (2017) for details about these products]. For the 2AKu-NS, only the NS footprints in the inner swath (i.e., the footprints 13–37), coincident with the Ms footprints, were selected. The analysis has been limited to those footprints categorized as liquid precipitation by DPR at NSL. The NSL (or first clutter-free bin—CFB) is defined as the first DPR bin, from the sea surface level, not affected by ground clutter. For this study, NSL is never lower than 500 m and can reach values higher than 6600 m depending mainly on the surface morphology and also on the position within the sensor swath. For some cases with a clearly detected BB, Watters et al. (2018) noticed a wrong identification of the NSL that was located at the same or higher altitude of BB. To take into account this problem, in this study, all the DPR data for which the difference between BB and CFB height

was lower than 500 m have been filtered out. This corresponds to discard about 22.7% of the DPR profiles of stratiform precipitation with BB clearly detected and about 5.7% of the whole dataset, evenly distributed over land and sea. A standard output of DPR products is also the rain type flag (e.g., stratiform, convective, and other, that is the precipitation not classified as either stratiform or convective). This flag, as well as the surface type flag (i.e., land, sea, and coast), has been used to classify the datasets based on precipitation and surface type. This study mainly focuses on stratiform/convective precipitation over the land/sea because, although the sample size for other/coast precipitation is not negligible (Table 17.1), the results do not show any peculiarity with respect to the stratiform/convective and land/sea analysis. Other DPR outputs concerning the BB characteristics (i.e., quality of BB detection, and BB height) and the height of CFB have also been used. The inter-comparison between DF- and SF-based DPR products refers to four standard outputs: the corrected reflectivity at both Ka- and Ku-band (Z_{Ka} and Z_{Ku} , respectively), the mean mass-weighted diameter (D_m), the normalized intercept (N_w), and the rainfall rate (R). The dataset used for this analysis has been created after that different thresholds have been applied. The first threshold has been set on the DF-based Ka- and Ku-band corrected reflectivity at DF-based NSL: the two values had to exceed 16 and 15 dBZ, respectively. In addition, only footprints reporting liquid precipitation phase according to the DF-based algorithm, always at DF-based NSL, were selected. These thresholds led to select more than 685,000 footprints. For the selected footprints the SF-based algorithms (both Ka- and Ku-only) give the same parameters (i.e., reflectivity at Ka- and Ku-band, rainfall rate, D_m , N_w , and NSL) as standard outputs but they might report missing data in correspondence of DF-selected profiles in the case of failure of SF-based algorithm. Therefore the sample size of DF versus SF_{Ka-only} and DF versus SF_{Ku-only} depends on the number of missing data at SF. Table 17.1 reports the sample size as function of both precipitation- and surface-type classification.

Table 17.1 Sample size according to dual-frequency precipitation radar precipitation- and surface-type classification.

		Precipitation type		
		<i>Stratiform</i>	<i>Convective</i>	<i>Other</i>
Surface type	Land	256,540	46,951	5931
	Sea	265,156	61,924	16,391
	Coast	26,295	5073	931

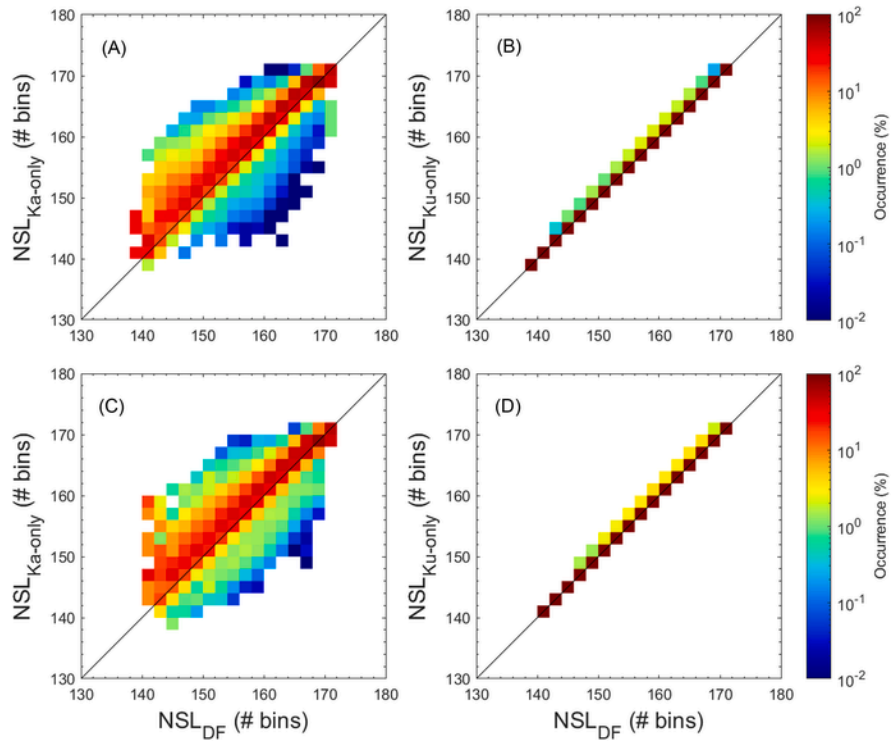
17.3.2 DF- AND SF-BASED DPR STANDARD OUTPUTS COMPARISON

As starting analysis the DF- and SF-based outputs used to select the data (i.e., precipitation phase, NSL, and BB properties) are compared. Table 17.2 reports the occurrence of the SF-based precipitation phase products when the DF-based precipitation phase detected liquid phase, as a function of surface and precipitation type at NSL. The results are divided for Ka- and Ku-only algorithm and for precipitation and surface type. The agreement in retrieving liquid precipitation phase between DF- and SF_{Ku-only}-based algorithms is almost total both for stratiform and convective precipitations, while it decreases for other precipitation types up to 77% over land showing better agreement both over sea and over coast. The agreement between DF- and SF_{Ka-only}-based algorithms is markedly lower. The DF- and SF_{Ka-only}-based algorithms agree in detecting the liquid-phase precipitation during stratiform events in a percentage ranging between 63.7% over land and 65.5% over coast. The remaining cases are almost all classified as “missing rain,” while a very negligible percentage of samples is classified as a mixed phase. A slight better agreement is obtained during convective precipitation, when the values increase up to 71% over land with slightly lower values over coast and over sea. The agreement for other precipitation types ranges between 16.7% (sea/coast) and 32% (land) with the majority of samples that are classified as missing precipitation by the SF_{Ka-only} algorithm. There are no cases where SF_{Ka/Ku-only}-based algorithm reports solid precipitation at the NSL when DF-based algorithm reports liquid precipitation.

Fig. 17.1 shows the 2-D density plot of NSL as identified by DF- and SF-based algorithms for stratiform (top row) and convective (bottom row) precipitation over land. The NSL is expressed as vertical bin number counted from the top, and so, the greater the bin number, the closer the surface. The color bar indicates the occurrence (%) of SF-based NSL (indicated in the y -axis) for each DF-based NSL bin (indicated in the x -axis, discretized in equally spaced intervals), normalized with respect to the total number of DF-based occurrences in each interval. The spread for stratiform precipitation between DF- and SF_{Ka-only}-based NSL (Fig. 17.1A) is marked with NSL generally greater (i.e., closer to the surface) for SF_{Ka-only}-based than DF-based with most of the points above the one-to-one line. On the other hand, there is no spread between DF- and SF_{Ku-only}-based NSL with almost all points on the one-to-one line (Fig. 17.1B). Not appreciable changes between DF- and SF_{Ku-only}-based NSL are notable during convective precipitation (Fig. 17.1D), while a slightly better agreement is obtained between DF- and SF_{Ka-only}-based NSL during convective than stratiform precipitation (Fig. 17.1C). It has to be remarked that the SF-based algorithm can sometimes report missing data at the DF-based NSL. This occurs exclusively for SF_{Ka-only}-based algorithm mainly because of the stronger attenuation affecting the Ka-band with respect to the Ku-band. These cases lead to different sample sizes when DF-based are compared with SF_{Ku-only}- and SF_{Ka-only}-based outputs, respectively. On average, the comparison between DF and

Table 17.2 Occurrence (%) of the single frequency–based precipitation phase products when the dual frequency–based precipitation phase detected liquid phase, as a function of surface and precipitation type at near-surface level.

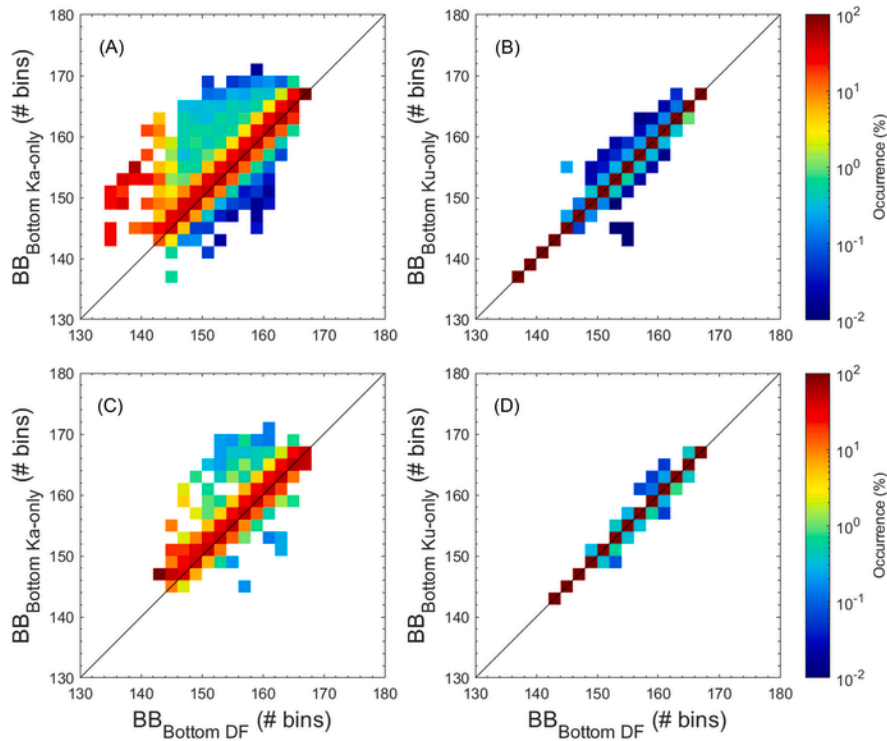
		Stratiform			Convective			Other		
		<i>Liquid</i>	<i>Mixed</i>	<i>Missing</i>	<i>Liquid</i>	<i>Mixed</i>	<i>Missing</i>	<i>Liquid</i>	<i>Mixed</i>	<i>Missing</i>
Land	Ka-only	63.7	0.5	35.8	71.4	1.1	27.5	32.3	0	67.7
	Ku-only	99.9	0.1	0	99.9	0.1	0	77.2	0	22.8
Sea	Ka-only	64.7	0.3	35.0	67.5	0.3	32.2	19.1	0	81.9
	Ku-only	99.9	0.1	0	99.9	0.1	0	88.4	0	11.6
Coast	Ka-only	65.5	0.4	34.1	69.4	0	30.6	16.7	0	83.3
	Ku-only	99.7	0.3	0	100	0	0	91.7	0	8.3

**FIGURE 17.1**

2-D density plots of NSL as identified by SF- and DF-based DPR algorithms over land during (top row) stratiform and (bottom row) convective precipitation. The color bar indicates the occurrence (%) of SF-based parameter values (indicated in the y-axis) for each DF-based parameter value (indicated in the x-axis, discretized in equally spaced intervals), normalized with respect to the total number of SF-based occurrences in each interval. *DF*, Dual-frequency; *DPR*, dual-frequency precipitation radar; *NSL*, near-surface level; *SF*, single-frequency.

$SF_{Ka-only}$ estimates is made on 40% of points less than the comparison between the DF and $SF_{Ku-only}$ estimates. Furthermore, for the cases when either Ku- or Ka-band radar measurements are missing (i.e., one of the SF product reports missing data), the DF estimates do not necessarily coincide with the results derived from the available SF-based measurements. In these cases, if the DF algorithm is able to reconstruct the vertical profile of both frequencies, the DF- and SF-based products are different; otherwise, the DF and SF products provide the same values of the retrieved parameters.

A similar analysis has been carried out for the detection of the BB bottom bin that is the level closest to the ground surface where the falling particles change their state from solid to liquid. Fig. 17.2 refers to stratiform precipitation over land on the top row and over sea on the bottom row (a negligible number of convective

**FIGURE 17.2**

2-D density plots of BB bottom as identified by SF- and DF-based DPR algorithms during stratiform precipitation (top row) over land and (bottom row) over the sea. The normalization and the color bar follow the description of Fig. 17.1. *BB*, Bright band; *DF*, dual-frequency; *DPR*, dual-frequency precipitation radar; *SF*, single-frequency.

samples reported a clear detected BB). The comparison between DF- and $SF_{Ka-only}$ -based BB bottom bin products evidences a significant spread more marked over land than over sea, even if the occurrence rapidly decreases moving away from the one-to one line (Fig. 17.2A and C). A clear offset of about 15 bins, over land (Fig. 17.2A), is shown when the DF-based BB bottom is estimated between bin 132 and 142. The difference between DF- and $SF_{Ku-only}$ -based is negligible both over land and over the sea (Fig. 17.2B and D).

17.4 DF- AND SF-BASED RAIN AND DSD PARAMETERS COMPARISON AT NSL

This paragraph focuses on the comparison between the integral (i.e., Z_{Ku} and Z_{Ka} and R) and the microphysical (i.e. D_m and N_w) DSD parameters derived from DF-

and SF-based DPR algorithm. Fig. 17.3 reports the 2-D density plots of NSL corrected Z_{Ka} and Z_{Ku} from the DF product 2ADPR-Ms and from the SF (both 2AKa-Ms and 2AKu-NS) products, for stratiform and convective precipitations over land. Fig. 17.3 and the three following figures (to) have the same layout of Fig. 17.1, which are the top and bottom rows refer to stratiform and convective precipitations, respectively, while the normalization is done with respect to the occurrence of each bin of the considered DF-based parameter. In addition, each panel reports also the sample size from which the 2-D density plot is obtained. Hereafter, Z_{Ka} (Z_{Ku}) derived from SF- and DF-based algorithms will be referred to $Z_{Ka-only}$ ($Z_{Ku-only}$) and Z_{Ka-DF} (Z_{Ku-DF}), respectively. The agreement between $Z_{Ka-only}$ and Z_{Ka-DF} for stratiform precipitation is rather good in the range between 22 and 35 dBZ (Fig. 17.3A) with most of the points around the one-to-one line. The agreement becomes

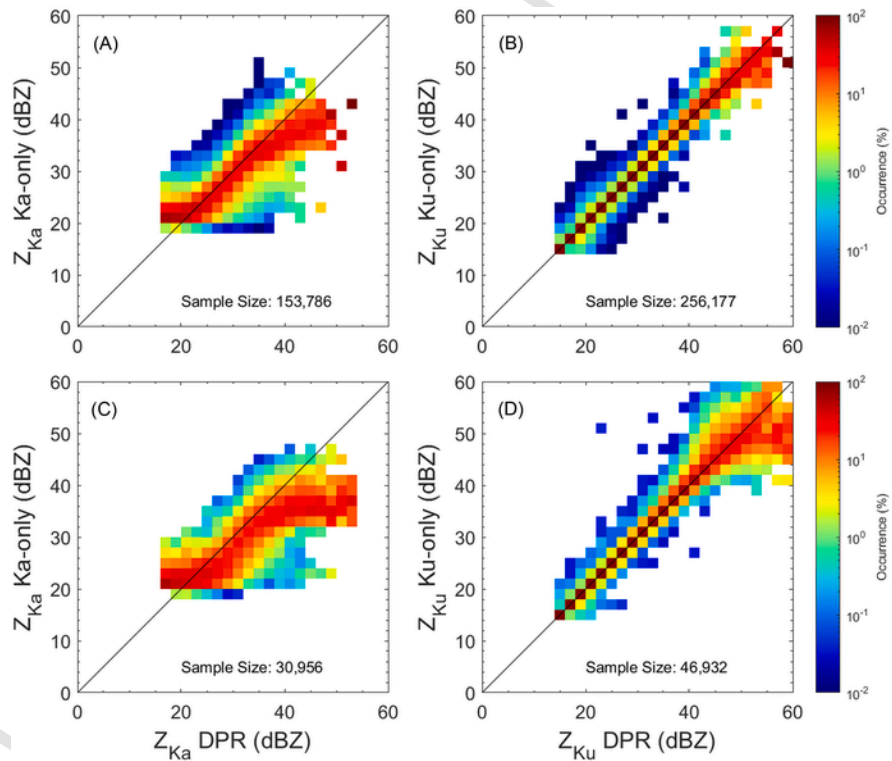


FIGURE 17.3

2-D density plots of $Z_{Ka/Ku}$ as corrected by DF-based DPR algorithm (x-axis) and by SF-based Ka-only/Ku-only DPR algorithm (y-axis, left and right columns, respectively) for (top row) stratiform and (bottom row) convective precipitation over land. The normalization and the color bar follow the description of Fig. 17.1. *DF*, Dual-frequency; *DPR*, dual-frequency precipitation radar; *SF*, single-frequency.

worse at lower and, in a more marked way, at higher Z values, where $Z_{\text{Ka-only}}$ generally overestimates and underestimates the $Z_{\text{Ka-DF}}$ values, respectively. $Z_{\text{Ku-only}}$ and $Z_{\text{Ku-DF}}$ show a better agreement with respect to the Ka-band for stratiform precipitation on the whole spectrum of Z values (Fig. 17.3B). The occurrence on the one-to-one line is generally higher than 90% (which means that the $Z_{\text{Ku-only}}$ and $Z_{\text{Ku-DF}}$ perfectly agree more than 90% of the times for most Z values), while slightly lower occurrence is obtained at high reflectivity (more than 40 dBZ). The results are not very different for convective precipitation, even if $Z_{\text{Ka-only}}$ shows constant lower values than $Z_{\text{Ka-DF}}$ except for very low values (Fig. 17.3C). The spread between $Z_{\text{Ku-only}}$ and $Z_{\text{Ku-DF}}$ is slightly larger for $Z_{\text{Ku}} > 40$ dBZ, highlighting different performances of the two correction methods in the case of heavy precipitation (Fig. 17.3D) related to the stronger attenuation suffered by Ka-band. The results obtained over sea and over coast (not shown) do not significantly differ from the results over land both for stratiform and convective precipitations.

The comparison looks quite different when D_m is analyzed, as shown in Fig. 17.4. Hereafter, D_m retrieved at SF and DF will be referred to as $D_m\text{-Ka}$ (for 2AKa-Ms), $D_m\text{-Ku}$ (for 2AKu-NS), and $D_m\text{-DF}$ (for 2ADPR-Ms), respectively. It is worth noticing the different D_m upper limits set to 3 mm for $D_m\text{-Ka}$ and $D_m\text{-DF}$, and 5 mm for $D_m\text{-Ku}$. Fig. 17.4A shows a high occurrence of $D_m\text{-Ka}$ between 1.0 and 1.4 mm when $D_m\text{-DF} < 1.2$ mm for stratiform precipitation. The agreement slightly improves for moderate D_m values, roughly ranging between 1.2 and 1.6 mm, where most of the points are very close to the one-to-one line. When $D_m\text{-DF}$ exceeds 1.6 mm, two clusters can be identified: one more marked and corresponding to $D_m\text{-Ka}$ equal to 3 mm (due to saturated D_m issue) and one where the $D_m\text{-Ka}$ values (ranging from 1.6 to 1.2 mm) are lower than $D_m\text{-DF}$. The D_m estimates are more similar when $D_m\text{-Ku}$ is compared with $D_m\text{-DF}$ (Fig. 17.4B) even if, similarly to Ka-only, $D_m\text{-Ku}$ is generally lower than $D_m\text{-DF}$ (the difference increases at higher $D_m\text{-DF}$ values). The analysis for convective precipitation parts (C and D) shows similar results but with a larger spread of the distributions. Moreover, $D_m\text{-Ku}$ shows slightly higher occurrence above the one-to-one line when $D_m\text{-DF}$ ranges between 0.5 and 1.3 mm (Fig. 17.4D). The two SF algorithms find most of the D_m between 0.8 and 1.6 mm (especially for stratiform precipitation), with a lack of values below 0.8 mm, while for larger D_m , the DF values are more correlated with the Ku estimates. Again, negligible differences are obtained over coast and over sea (not shown), even if a slight improvement in the agreement can be evidenced.

The agreement between SF- and DF-based algorithms is worse for N_w . Fig. 17.5 evidences that the SF-based $\log(N_w)$ estimates, for both Ka- and Ku-only products, [$\log(N_w\text{-Ka})$, and $\log(N_w\text{-Ku})$, respectively] are basically always around $3.2 \text{ m}^{-3} \text{ mm}^{-1}$ regardless of the $\log(N_w)$ DF values [$\log(N_w\text{-DF})$]. This is true for both stratiform and convective precipitations. The comparison between $\log(N_w\text{-Ka})$ and $\log(N_w\text{-DF})$ shows a second cluster of occurrence for $\log(N_w\text{-Ka})$ around $2 \text{ m}^{-3} \text{ mm}^{-1}$ and $\log(N_w\text{-DF})$ ranging between 2.5 (2) and $4 \text{ m}^{-3} \text{ mm}^{-1}$ for stratiform (convective) precipitation (Fig. 17.5A and C). The disagreement is not surprising,

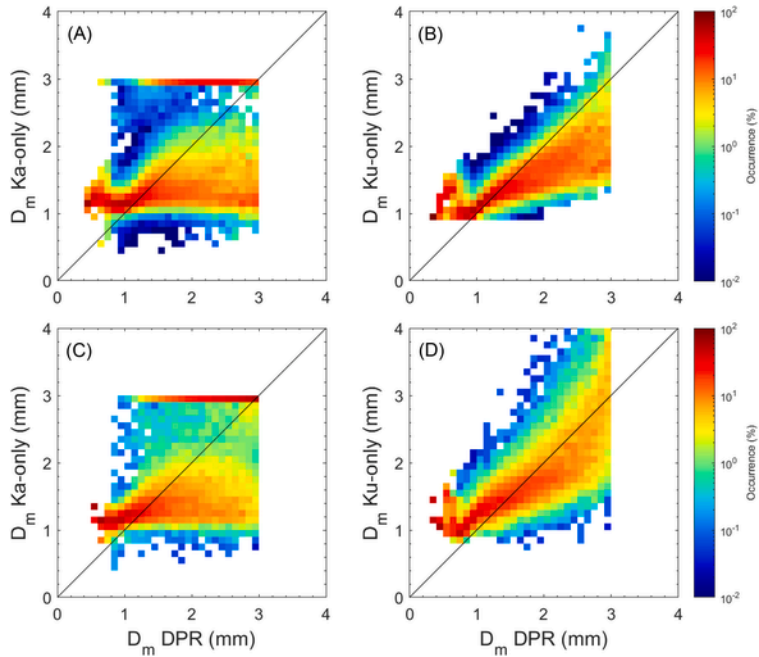
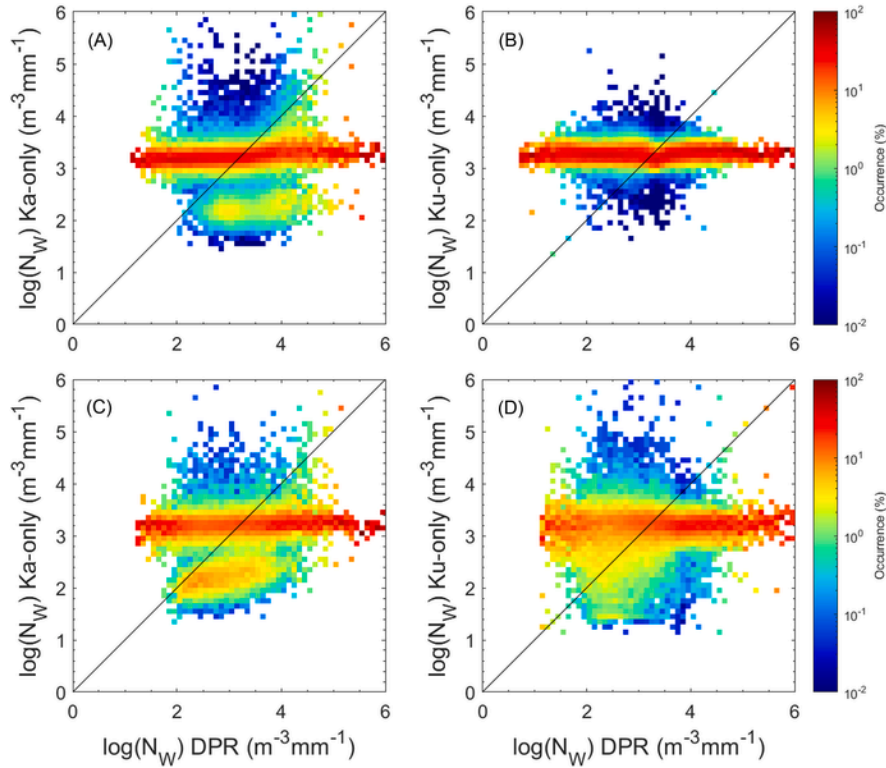


FIGURE 17.4

2-D density plots of D_m as estimated by DF-based DPR algorithm (x-axis) and by SF-based Ka-only/Ku-only DPR algorithm (y-axis, left and right columns, respectively) for (top row) stratiform and (bottom row) convective precipitation over land. The normalization and the color bar follow the description of Fig. 17.1. *DF*, Dual-frequency; *DPR*, dual-frequency precipitation radar; *SF*, single-frequency.

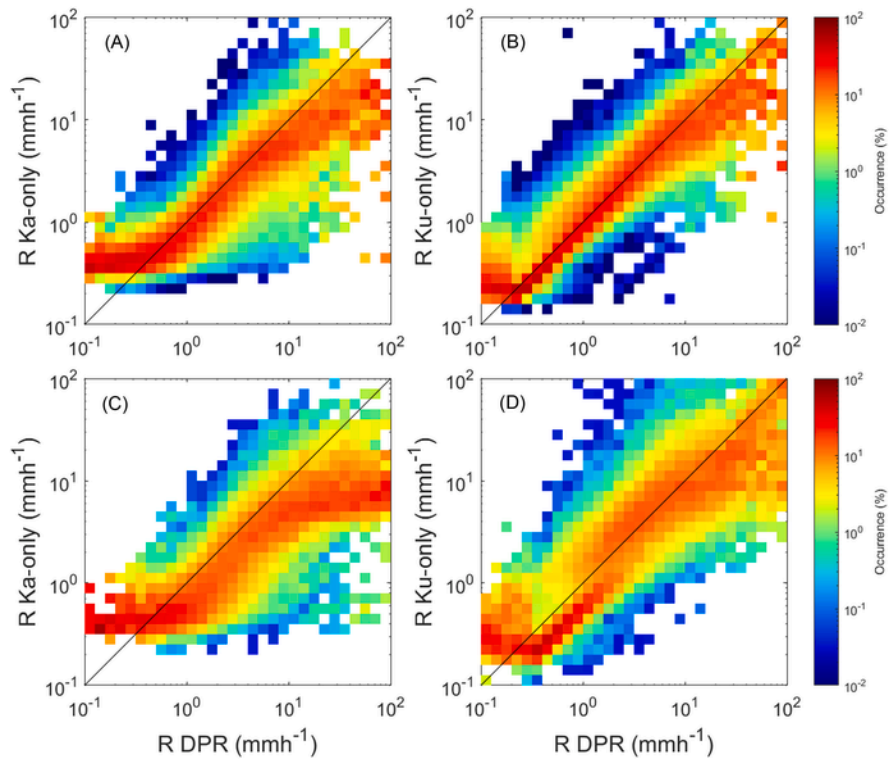
cause a sensitivity study (not shown) shows a very narrow distribution of $\log(N_w)$ for SF-based DPR products with the peak position centered around $3.2 \text{ m}^{-3} \text{ mm}^{-1}$. Any SF estimate is not able to describe the variability of N_w , making it necessary to use the DF algorithm.

In conclusion of this section, the 2-D density plot obtained for rainfall rate is shown in Fig. 17.6. In general, the behavior is similar to that shown by the corrected reflectivity (Fig. 17.3), even if some differences are evident especially for the comparison between R values at Ku-only (R_{Ku}) and DF (R_{DF}). The agreement is still good for stratiform precipitation (Fig. 17.6B) but the occurrence on the one-to-one line is not as high as for Z , not exceeding 30% at the most (decreasing when moving away from the one-to-one line). For stratiform precipitation, R for Ka-only (R_{Ka}) shows values very similar to R_{DF} between 1 and 20 mm h^{-1} , while for higher values the difference is larger with a general underestimation of R_{Ka} with respect to R_{DF} (Fig. 17.6A). For convective precipitation, R_{Ka} is generally lower than R_{DF} , over the whole spectrum of rain intensity (Fig. 17.6C), while the agreement be-

**FIGURE 17.5**

2-D density plots of N_w as estimated by DF-based DPR algorithm (x-axis) and by SF-based Ka-only/Ku-only DPR algorithm (y-axis, left and right columns, respectively) for (top row) stratiform and (bottom row) convective precipitation over land. The normalization and the color bar follow the description of Fig. 17.1. *DF*, dual-frequency; *DPR*, dual-frequency precipitation radar; *SF*, single-frequency.

tween R_{Ku} and R_{DF} is better (from low to heavy rain intensity, between 0.8 and 30 mm h⁻¹—Fig. 17.6D). A cluster of R_{Ku} values lower than R_{DF} is found between 0.3 and 2 mm h⁻¹ (Fig. 17.6D), while all four plots show SF-based R values higher than DF-based R values at very low rain rates (between 0.1 and 0.3 mm h⁻¹). This feature can be partially explained by the fact that, nominally, the minimum measurable rain rate is set to 0.5 and 0.2 mm h⁻¹ at Ku- and Ka-band, respectively, while no lower limit is given for the DF outputs (Iguchi, 2017). We analyzed the two clusters (one for Ka- and one for Ku-band) more in-depth. We selected the samples satisfying $R_{DF} < 0.2$ mm h⁻¹ and $0.2 < R_{Ku} < 0.7$ mm h⁻¹ for Ku-band, and the samples satisfying $R_{DF} < 0.3$ mm h⁻¹ and $0.3 < R_{Ka} < 0.7$ mm h⁻¹ for Ka-band, respectively. Then, for these samples, the reflectivity measured at Ku- and Ka-band has been compared. Since the samples fall in the Rayleigh region, the reflectivity measured by DPR is

**FIGURE 17.6**

2-D density plots of R as estimated by DF-based DPR algorithm (x -axis) and by SF-based Ka-only/Ku-only DPR algorithm (y -axis, left and right columns, respectively) for (top row) stratiform and (bottom row) convective precipitation over land. The normalization and the color bar follow the description of Fig. 17.1. *DF*, Dual-frequency; *DPR*, dual-frequency precipitation radar; *SF*, single-frequency.

the same at Ka- and Ku-band (all the points are on the one-to-one line, not shown). Thus the reflectivity corrected by the DF and Ku-/Ka-only algorithm has been compared. Although most of the points at Ku-band are on the one-to-one line (not shown), the R given by the two algorithms are always different. On the other hand, the reflectivity corrected by the SF Ka-only algorithm is generally higher than the reflectivity corrected by the DF algorithm. The differences found in the corrected reflectivity and in R can be connected to the assumptions made in the different algorithms. The corresponding analysis of the four parameters carried out over sea shows a comparable behavior with respect to the one over land for both precipitation types (stratiform and convective) and for both the SF-based products (Ka-/Ku-only) with respect to the DF-based product. The width of the distribution over sea (not shown) is generally smaller, highlighting that the attenuation correction [sur-

face reference technique (SRT) and DF SRT] is more accurate over sea than over land (Meneghini et al., 2015).

A more quantitative evaluation of the difference between the considered parameters as estimated by SF- and DF-based algorithms is provided through the computation of some statistical scores, namely, mean difference (MD) and root mean square difference (RMSD) (Nurmi, 2003). The trend of MD and RMSD as a function of the DF-based parameter values (e.g., the trend of Z_{Ka} MD with respect to the Z_{Ka} -DF values) for different surface types (land/sea) and precipitation types (stratiform/convective) both for Ka-only (2AKa-Ms) and Ku-only (2AKu-NS) is reported in Fig. 17.7, respectively. Furthermore, the overall means of MD and RMSD for each surface and precipitation type combination are reported in each panel of Fig. 17.7. At Ka-band the overall MD generally shows negative values, both for stratiform and convective precipitations and both over land and over sea, indicating lower estimates of SF-based algorithm with respect to the DF-based algorithm on average (Fig. 17.7A–D). The only positive values of MD at Ka-band are found for D_m for stratiform precipitation and can be related to the saturation issue in Ka-only (i.e., overestimation of the path integrated attenuation leading to D_m values larger than 3 mm, which are consequently set to 3 mm being this the D_m upper limits at SF Ka-only). At Ku-band the MD is generally very close to zero for stratiform precipitation, thus evidencing the similarity between DF and Ku-only products (Fig. 17.7E–H). For convective precipitation the MD is mainly positive [it is negative only for $\log(N_w)$]. Although the overall means summarize the behavior of SF-based

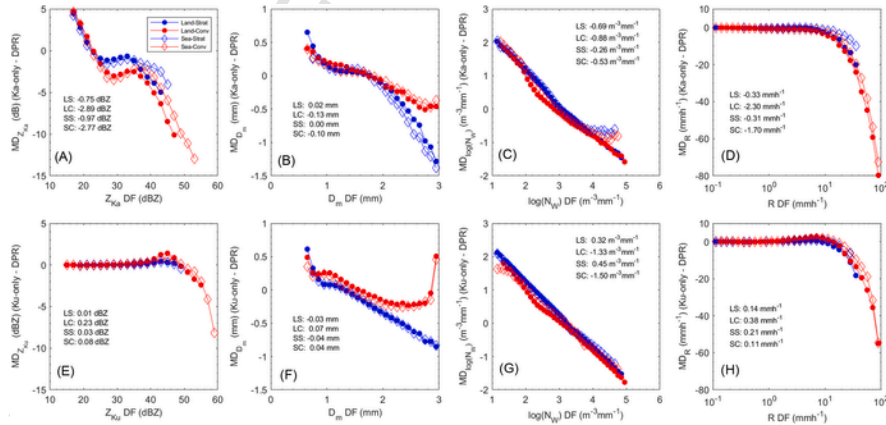


FIGURE 17.7

Trend of MD with respect to the four parameters analyzed [i.e., (A)–(E) Z , (B)–(F) D_m , (C)–(G) $\log(N_w)$, and (D)–(H) R] for (top row) Ka-band and (bottom row) Ku-band. The blue/red lines refer to stratiform/convective precipitation, while the dot/diamond symbols refer to the land/sea. The LS, LC, SS, and SC acronyms report the overall mean MD for land stratiform, land convective, sea stratiform, and sea convective combinations, respectively. MD, Mean difference.

products, the analysis of the plots reveals more specific trends. Fig. 17.7A shows that Z_{Ka} MD moves from slightly positive to largely negative (mainly for convective precipitation) values from lower to higher DF Z_{Ka} . Between 25 and 35 dBZ, MD is closer to zero for stratiform precipitation than for convective precipitation. The plot also shows that strong attenuation at Ka-band plays a role at $Z_{\text{Ka}} > 35$ dBZ, where the lost signal mirrors in negative MD (up to -13 dB during convective precipitation over sea). On the other hand, MD is around 0 dB for $Z_{\text{Ku}} < 45$ dBZ and then it assumes negative values up to -8 dB (Fig. 17.7E). The D_m MD at Ka-band follows the same trend of Z_{Ka} MD with values around zero for $1 \text{ mm} < D_m < 2 \text{ mm}$ and more marked underestimation of D_m -Ka for stratiform than for convective precipitation at higher D_m values (Fig. 17.7B). A similar trend is shown by D_m MD at Ku-band with higher values for convective than stratiform precipitations, excluding very low D_m (Fig. 17.7F). Although the trend of Z_{Ku} MD is around 0 dB except that for very high Z_{Ku} values, the trend of D_m MD suggests an overestimation of medium drops for convective precipitation by the SF_{Ku-only} algorithm leading to positive MD up to $D_m < 1.6 \text{ mm}$ and an underestimation of medium/large drops for larger D_m values leading to greater negative MD. This behavior is more marked during stratiform with respect to convective precipitation. The $\log(N_w)$ MD shows a linear trend moving from positive to negative values at lower and higher $\log(N_w)$, respectively, both at Ka- and Ku-band (Fig. 17.7C and G). This is explained by the very narrow distribution of $\log(N_w)$ values at SF algorithms. On the other hand, the trends of R MD at Ka- and Ku-band are quite similar to each other and they both follow the trend of Z_{Ku} MD. R MD is close to 0 mm h^{-1} for low-to-moderate R (MD is slightly positive for convective precipitation at Ku-band for $1 \text{ mm h}^{-1} < R < 10 \text{ mm h}^{-1}$) becoming negative for moderate to heavy rain intensity both for stratiform and convective precipitations. For very heavy precipitation (registered mainly during convective events), R MD for Ka-band reaches significantly lower values (around -80 mm h^{-1}) than for Ku-band (around -50 mm h^{-1}).

The RMSD shows not negligible differences between convective and stratiform precipitation for some parameters or for some range of values of the considered parameter at both Ka- and Ku-band, confirming the larger uncertainties of the SF- and DF-based DPR algorithms in case of heavy precipitation (blue and red curves in Fig. 17.8); this is true over land and over sea. On the other hand, the D_m RMSD is higher during stratiform than convective precipitation for $D_m > 2.0 \text{ mm}$ about both at Ka- (Fig. 17.8B) and Ku-band (Fig. 17.8F); this is also true for very low D_m values. Both MD and RMSD generally show slightly lower values over the sea than over land for all parameters considered (diamond red vs dotted red lines in Figs. 17.7 and 17.8) confirming the better attenuation correction over the sea than over land.

The availability of the large dataset (i.e., 5 years of data) allowed to perform a seasonal analysis in term of statistical indicators as a function of both precipitation and surface type ensuring an enough number of samples for each subset of data. In addition to MD and RMSD reported in Figs. 17.7 and 17.8 (calculated for the whole dataset), Table 17.3 reports also the fractional standard difference (FSD), expressed in percent, that is the ratio between the RMSD and the mean value of the

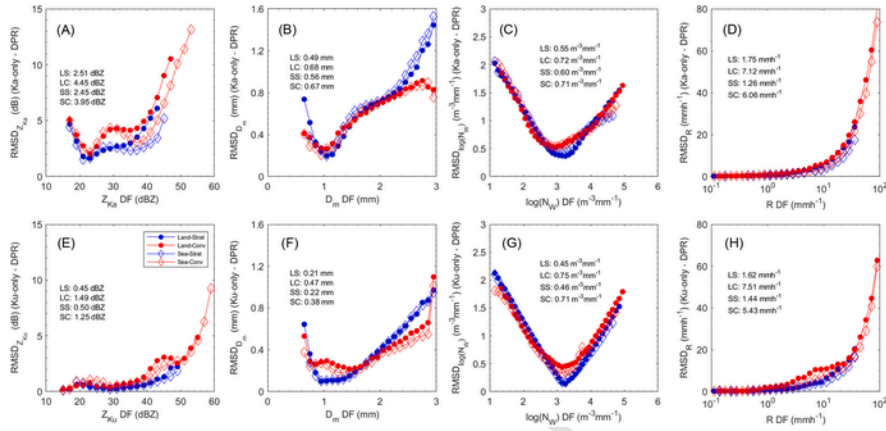


FIGURE 17.8

Trend of RMSD with respect to the four parameters analyzed [i.e., (A)–(E) Z , (B)–(F) D_m , (C)–(G) $\log(N_w)$, and (D)–(H) R] for (top row) Ka-band and (bottom row) Ku-band. The blue/red lines refer to stratiform/convective precipitation, while the dot/diamond symbols refer to the land/sea. The LS, LC, SS, and SC acronyms report the overall mean RMSD for land stratiform, land convective, sea stratiform, and sea convective combinations, respectively. *RMSD*, Root mean square difference.

reference data (i.e., the DF-based parameters) for stratiform and convective precipitations, respectively. The four seasons are divided as follows: winter (December–January–February), spring (March–April–May), summer (June–July–August), and fall (September–October–November). Table 17.3 confirms that, during stratiform precipitation, $Z_{Ku-only}$ and Z_{Ku-DF} provide very similar values regardless the season with MD always close to zero; at the same time the very low RMSD and FSD values (the highest values are reached in the summer) highlight the limited spread of the distribution. On the other hand, the SF algorithm underestimates the reflectivity at Ka-band for all the seasons with MD values improving from winter to fall; in this case, both RMSD and FSD present higher values showing the maximum during summer. The analysis of D_m reveals that SF algorithm at Ku-band generally underestimates the parameter showing very slight negative MD values never exceeding -0.06 mm, while D_m -Ka is lower (higher) than D_m -DF during winter and spring (summer and fall). The RMSD oscillates around 0.2 and 0.5 mm at Ku- and Ka-band, respectively, with a wider range for the latter frequency. N_w MD has a symmetrical behavior with respect to D_m both at Ka- and at Ku-band where it assumes high positive values. Finally, the R MD is negative (positive) at Ka-band (Ku-band) regardless the season. Although the absolute values are larger at Ka- than Ku-band, both RMSD and FSD show very close values at the two frequencies evidencing different shape of the two distributions. At the same time the analysis of the statistical scores does not allow to deduce a better agreement between SF and DF algorithms

Table 17.3 Seasonal analysis of mean difference (MD), root mean square difference (RMSD), and fractional standard difference (FSD) as a function of precipitation and surface type for stratiform precipitation.

		Stratiform						
		Winter						
		Z_{Ka} (dB)	Z_{Ku} (dB)	D_{mKA} (mm)	D_{mKU} (mm)	N_{wKA} ($m^{-3} mm^{-1}$)	N_{wKU} ($m^{-3} mm^{-1}$)	R_{Ka} ($mm h^{-1}$)
MD	Land	-1.18	0.01	-0.12	-0.06	0.83	0.92	-0.45
	Sea	-1.32	0.03	-0.16	-0.06	1.30	0.69	-0.37
	Coast	-1.15	0.01	-0.15	-0.05	1.10	0.63	-0.30
RMSD	Land	2.56	0.41	0.45	0.24	0.54	0.50	1.56
	Sea	2.38	0.42	0.50	0.24	0.56	0.50	1.04
	Coast	2.70	0.41	0.44	0.24	0.51	0.50	1.75
FSD (%)	Land	8.95	1.33	32.01	16.76	1.61	1.48	15.29
	Sea	8.39	1.34	34.87	16.96	1.72	1.55	2.14
	Coast	9.52	1.33	31.34	17.18	1.55	1.51	3.88
		Spring						
		Z_{Ka} (dB)	Z_{Ku} (dB)	D_{mKA} (mm)	D_{mKU} (mm)	N_{wKA} ($m^{-3} mm^{-1}$)	N_{wKU} ($m^{-3} mm^{-1}$)	R_{Ka} ($mm h^{-1}$)
MD	Land	-0.97	0.01	-0.11	-0.06	0.76	0.79	-0.38
	Sea	-0.99	0.02	-0.09	-0.05	0.59	0.54	-0.31
	Coast	-0.95	0.02	-0.10	-0.04	0.62	0.41	-0.19
RMSD	Land	2.40	0.40	0.45	0.23	0.52	0.48	1.14
	Sea	2.17	0.41	0.48	0.22	0.54	0.46	0.89
	Coast	2.51	0.40	0.43	0.22	0.52	0.48	2.95
FSD (%)	Land	8.56	1.32	32.42	16.37	1.57	1.46	34.00
	Sea	7.73	1.35	35.11	16.06	1.63	1.38	3.60
	Coast	8.85	1.31	31.59	16.47	1.45	1.36	113.94
		Summer						
		Z_{Ka} (dB)	Z_{Ku} (dB)	D_{mKA} (mm)	D_{mKU} (mm)	N_{wKA} ($m^{-3} mm^{-1}$)	N_{wKU} ($m^{-3} mm^{-1}$)	R_{Ka} ($mm h^{-1}$)
MD	Land	-0.85	0.01	0.03	-0.02	-1.08	0.01	-0.36

Table 17.3 (Continued)

		Stratiform						
		Winter						
		Z_{Ka} (dB)	Z_{Ku} (dB)	D_{mKa} (mm)	D_{mKu} (mm)	N_{wKa} ($m^{-3} mm^{-1}$)	N_{wKu} ($m^{-3} mm^{-1}$)	R_{Ka} ($mm h^{-1}$)
RMSD	Sea	-0.50	0.04	0.07	-0.04	-0.86	0.47	-0.26
	Coast	-0.38	0.01	0.11	0.01	-1.62	-0.54	-0.15
	Land	2.74	0.46	0.51	0.22	0.57	0.47	1.63
FSD (%)	Sea	2.73	0.64	0.58	0.20	0.63	0.43	1.03
	Coast	2.97	0.65	0.52	0.18	0.54	0.42	2.37
	Land	9.69	1.54	38.38	16.89	1.63	1.35	6.56
MD	Sea	9.76	2.13	46.22	16.39	1.86	1.29	3.60
	Coast	10.48	2.22	42.23	14.66	1.58	1.21	14.38
	Fall							
		Z_{Ka} (dB)	Z_{Ku} (dB)	D_{mKa} (mm)	D_{mKu} (mm)	N_{wKa} ($m^{-3} mm^{-1}$)	N_{wKu} ($m^{-3} mm^{-1}$)	R_{Ka} ($mm h^{-1}$)
RMSD	Land	-0.54	0.01	0.09	-0.03	-1.31	0.22	-0.28
	Sea	-0.67	0.06	0.17	-0.05	-1.64	0.71	-0.25
	Coast	-0.35	0.01	0.09	-0.02	-1.32	-0.09	-0.24
FSD (%)	Land	2.48	0.47	0.53	0.21	0.57	0.44	2.14
	Sea	2.61	0.68	0.67	0.23	0.69	0.47	2.08
	Coast	2.96	0.64	0.51	0.21	0.55	0.46	3.64
MD	Land	8.35	1.47	39.59	15.47	1.63	1.26	4.07
	Sea	8.50	2.02	48.29	16.22	2.04	1.38	3.57
	Coast	9.57	1.85	38.49	16.18	1.50	1.28	6.53

over land or over sea because the values are close to each other and in some cases are better over land while in other cases are better over sea, but the scores are worse over coast.

The seasonal analysis for the convective precipitation (Table 17.4) shows not only some similarities but also some differences with respect to the stratiform precipitation. There is a worsening of both Z_{Ka} MD and Z_{Ku} MD, more marked at Ka-band where the values are always lower than -2 dB reaching almost -3.5 dB during summer. The RMSD and the FSD also worsen increasing by about 150% with respect to the stratiform precipitation. D_m MD at Ka-band is negative for all the sea-

Table 17.4 Seasonal analysis of mean difference (MD), root mean square difference (RMSD), and fractional standard difference (FSD) as a function of precipitation and surface type for convective precipitation.

		Convective						
		Winter						
		Z_{Ka} (dB)	Z_{Ku} (dB)	D_{mKA} (mm)	D_{mKU} (mm)	N_{wKA} ($m^{-3} mm^{-1}$)	N_{wKU} ($m^{-3} mm^{-1}$)	R_{Ka} ($mm h^{-1}$)
MD	Land	-2.41	0.03	-0.04	0.01	-1.59	-1.05	-1.61
	Sea	-2.77	0.08	-0.12	0.01	-0.67	-0.96	-1.46
	Coast	-2.31	0.09	-0.08	0.01	-1.22	-1.32	-1.23
RMSD	Land	3.90	0.70	0.55	0.30	0.64	0.63	5.99
	Sea	3.66	0.69	0.59	0.32	0.60	0.63	3.69
	Coast	4.00	0.58	0.48	0.30	0.60	0.67	5.25
FSD (%)	Land	11.64	1.81	34.86	19.29	1.73	1.69	9.87
	Sea	11.00	1.78	35.16	18.87	1.68	1.77	6.44
	Coast	11.96	1.49	30.11	18.90	1.59	1.78	20.94
		Spring						
		Z_{Ka} (dB)	Z_{Ku} (dB)	D_{mKA} (mm)	D_{mKU} (mm)	N_{wKA} ($m^{-3} mm^{-1}$)	N_{wKU} ($m^{-3} mm^{-1}$)	R_{Ka} ($mm h^{-1}$)
MD	Land	-2.18	0.10	-0.02	-0.01	-1.84	-0.63	-1.30
	Sea	-2.48	0.09	-0.15	0.01	-0.04	-1.02	-1.45
	Coast	-2.37	0.10	-0.08	0.04	-1.77	-1.73	-1.58
RMSD	Land	3.73	0.65	0.52	0.32	0.63	0.64	3.91
	Sea	3.60	0.81	0.58	0.35	0.60	0.64	4.87
	Coast	3.98	0.85	0.54	0.29	0.66	0.66	7.48
FSD (%)	Land	11.36	1.75	32.90	20.25	1.69	1.70	16.98
	Sea	10.76	2.05	35.48	21.45	1.68	1.79	7.82
	Coast	12.08	2.25	35.51	19.50	1.70	1.68	10.34
		Summer						
		Z_{Ka} (dB)	Z_{Ku} (dB)	D_{mKA} (mm)	D_{mKU} (mm)	N_{wKA} ($m^{-3} mm^{-1}$)	N_{wKU} ($m^{-3} mm^{-1}$)	R_{Ka} ($mm h^{-1}$)
MD	Land	-3.22	0.36	-0.22	0.09	-0.21	-1.35	-2.46

Table 17.4 (Continued)

		Convective						
		Winter						
		Z_{Ka} (dB)	Z_{Ku} (dB)	D_{mKa} (mm)	D_{mKu} (mm)	N_{wKa} ($m^{-3} mm^{-1}$)	N_{wKu} ($m^{-3} mm^{-1}$)	R_{Ka} ($mm h^{-1}$)
RMSD	Sea	-2.41	0.08	-0.14	0.04	0.32	-1.79	-0.93
	Coast	-3.46	0.17	-0.15	0.08	-0.80	-2.27	-3.14
	Land	4.70	1.65	0.74	0.54	0.74	0.81	7.10
	Sea	3.93	1.14	0.75	0.34	0.75	0.75	4.03
FSD (%)	Coast	5.66	1.73	0.74	0.41	0.75	0.81	11.87
	Land	13.82	4.05	38.49	28.22	1.92	2.12	10.96
	Sea	12.72	3.07	56.61	25.63	2.03	2.02	7.14
	Coast	15.85	4.09	44.07	24.55	1.98	2.12	16.64
		Fall						
		Z_{Ka} (dB)	Z_{Ku} (dB)	D_{mKa} (mm)	D_{mKu} (mm)	N_{wKa} ($m^{-3} mm^{-1}$)	N_{wKu} ($m^{-3} mm^{-1}$)	R_{Ka} ($mm h^{-1}$)
MD	Land	-3.13	0.12	-0.14	0.06	-0.90	-1.43	-2.84
	Sea	-2.74	0.08	-0.07	0.06	-0.49	-1.62	-2.21
	Coast	-3.02	0.30	-0.06	0.02	-1.49	-0.92	-3.77
RMSD	Land	4.64	1.50	0.71	0.46	0.76	0.79	8.69
	Sea	4.27	1.74	0.73	0.42	0.81	0.74	8.40
	Coast	5.43	2.39	0.75	0.42	0.83	0.81	13.76
FSD (%)	Land	13.17	3.62	40.57	26.67	2.03	2.10	12.85
	Sea	11.74	3.99	44.81	25.80	2.19	2.02	12.34
	Coast	14.47	5.39	43.33	24.14	2.07	2.03	18.01

sons, evidencing a different trend with respect to the stratiform precipitation, while it is slightly positive at Ku-band. The D_m RMSD ranges between 0.55 mm about during winter/spring season to 0.75 mm about of summer/fall season at Ka-band, while lower values are obtained at Ku-band. A completely different result, if compared to the stratiform precipitation, is obtained for N_w MD that is always negative at both Ka- and Ku-band with a worsening of the absolute value at both frequencies. This trend is confirmed by RMSD and FSD. On the other hand, the R MD for convective precipitation follows R MD for stratiform precipitation with negative and positive values at Ka- and Ku-band, respectively (negative R MD are obtained at Ku-band for the fall season). Quite higher values of RMSD and FSD at both fre-

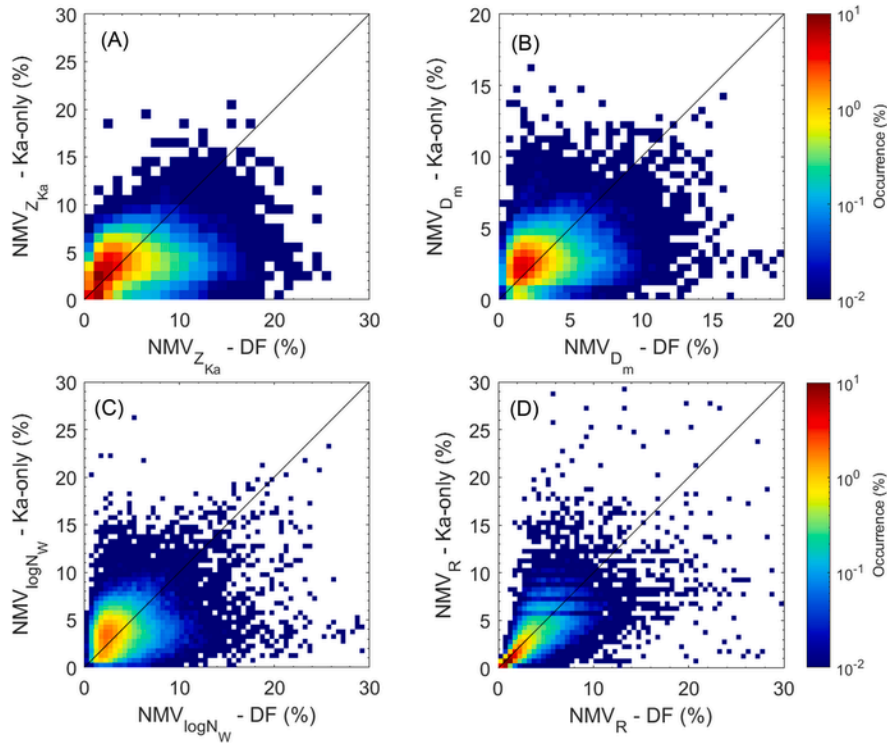
quencies confirm, one more time, the difficulties of SF-based products to correctly detect heavy precipitation.

To conclude the intercomparison between SF- and DF-based DPR products, the variability of Z and DSD parameter along vertical profiles is analyzed. Only profiles where the BB was clearly detected by both the Ka and Ku measurements have been considered, to analyze the profile from the BB bottom bin to the NSL bin to focus on liquid precipitation only. The cases were selected according to the “quality BB” variable in the DPR products. Furthermore, the thresholds on corrected Z_{DF} values at Ka- and Ku-band (i.e., 16 and 15 dBZ, respectively) at NSL have also been considered. This corresponds to analyze only stratiform precipitation because only a few of convective samples reporting clear BB satisfied the abovementioned conditions on reflectivity and are, consequently, not considered. To quantify the difference in reconstructing the vertical profile by the SF and DF algorithms, the normalized mean variance (NMV) of the four parameters (i.e., Z , D_m , N_w , and R) estimated by SF- and DF-based algorithms in the vertical profile considered has been computed. The NMV is defined in percent values as follows:

$$NMV_X = \sqrt{\frac{1}{N} \sum_{i=1}^N \frac{(X_{i,SF/DF} - \bar{X}_{SF/DF})^2}{\bar{X}_{SF/DF}}}$$

where N is the number of gates along the vertical profile, $X_{i,SF/DF}$ are the four parameters (i.e., Z , D_m , N_w , and R) estimated by SF-/DF-based algorithms, and $\bar{X}_{SF/DF}$ is the mean value of the considered parameter along the vertical profile. In particular, Fig. 17.9 shows the density plots of the DF NMV _{X} (2ADPR-Ms) versus the Ka-only NMV _{X} (2AKa-Ms) for stratiform precipitation over land. The 2-D density plot for NMV _{Z_{Ka}} shows that most of the samples are on the one-to-one line, even if a limited number of samples present DF-based NMV _{Z_{Ka}} up to 15% while the SF-based NMV _{Z_{Ka}} does not exceed 5% (Fig. 17.9A). The analysis of D_m shows a small vertical profile variability at both SF and DF, with almost the totality of the observations reporting NMV _{D_m} lower than 10% and most of samples with NMV _{D_m} < 5% (Fig. 17.9B). The distribution of NMV _{$\log(N_w)$} does not differ too much from the distribution of NMV _{D_m} (Fig. 17.9C). Its vertical variability does not exceed 15% for most cases. The variability of R does not present a different trend with respect to the other parameters, with a symmetrical distribution with respect to the one-to-one line (Fig. 17.9D).

Fig. 17.10 is the same as Fig. 17.9, but it refers to the Ku-band. If compared to the Ka-band, all the four parameters are on the one-to-one line with a rather limited spread. However, the range of NMV at Ku-band is generally larger than at Ka-band, with values reaching 50% in a not negligible number of cases for NMV _{Z_{Ku}} (Figs. 17.10A) or 25% for NMV _{R} (Fig. 17.10D). The structure below the melting layer as seen by DF algorithm seems to be almost fully described by the Ku-band, while the Ka-band contribution is very limited, probably due to the attenuation and

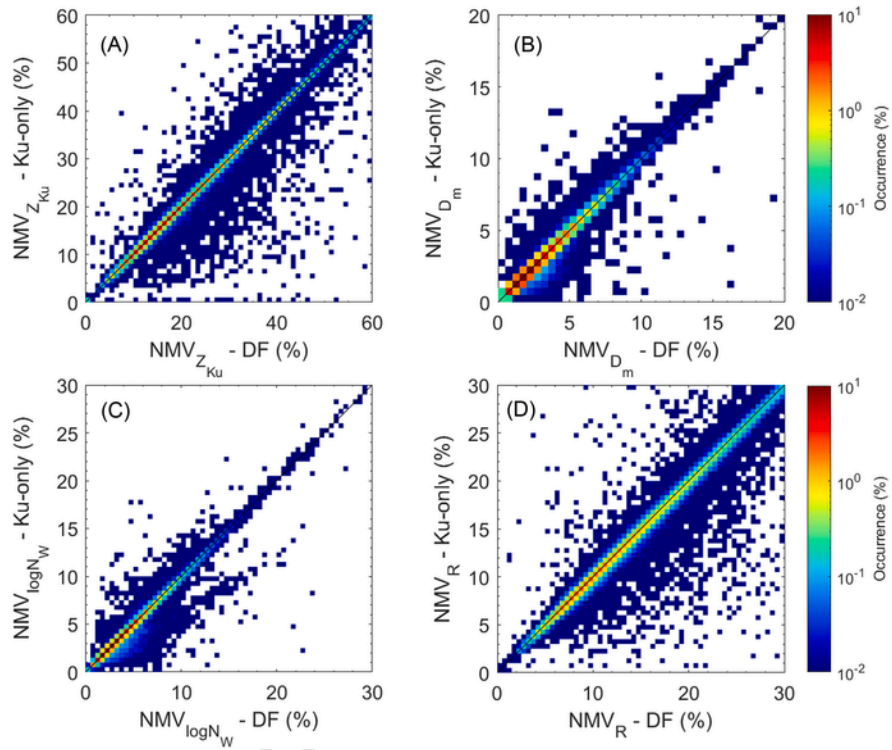
**FIGURE 17.9**

2-D density plots of NMV for the four analyzed parameters [i.e., (A) Z , (B) D_m , (C) $\log(N_w)$, and (D) R] as estimated by DF-based DPR algorithm (x-axis) and by SF-based Ka-only DPR algorithm (y-axis, left and right columns, respectively) for stratiform precipitation over land. *DF*, Dual-frequency; *DPR*, dual-frequency precipitation radar; *NMV*, normalized mean variance; *SF*, single-frequency.

to the fact that the correction algorithm is not able to reconstruct the profile below the BB.

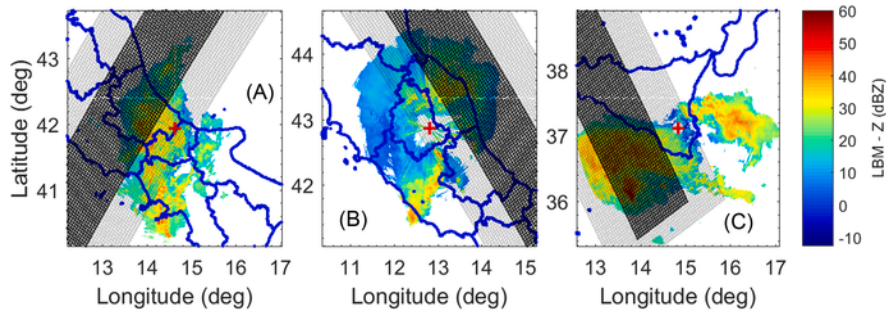
17.5 VALIDATION OF MICROPHYSICAL AND INTEGRAL DSD PARAMETERS

The second part of the chapter focuses on the validation of microphysical (i.e., mean mass-weighted diameter, normalized intercept) and integral parameters of the DSD (i.e., rainfall rate) over Italy. The validation is performed through a comparison between the DPR/DPR-GMI and the Italian GR network estimates for 42 selected GPM overpasses. As already highlighted in Section 17.2.2, the GR LBM has been taken as reference and compared with the DPR/DPR-GMI estimates at the

**FIGURE 17.10**

2-D density plots of NMV for the four analyzed parameters [i.e., (A) Z , (B) D_m , (C) $\log(N_w)$, and (D) R] as estimated by DF-based DPR algorithm (x-axis) and by SF-based Ku-only DPR algorithm (y-axis, left and right columns, respectively) for stratiform precipitation over land. *DF*, dual-frequency; *DPR*, dual-frequency precipitation radar; *NMV*, normalized mean variance; *SF*, single-frequency.

same altitude. As an example, Fig. 17.11 shows the GR LBM reflectivity measurements overlapped by corresponding GPM overpasses for parts (A) Il Monte, (B) Serano, and (C) Lauro sites. The gray area represents the Ku-band swath, and the black area represents the Ka-band swath, while the dots indicate the center of each footprint. The red plus sign indicates the location of the GR. It has to be highlighted that the GR pixels and DPR footprints used in the validation analysis are only those reporting liquid precipitation (as identified by DPR) at the NSL. In addition, the samples have been divided according to the surface (land and sea) and precipitation (stratiform and convective) type as classified by the DPR.

**FIGURE 17.11**

Example of three LBM reflectivities as measured by GR overlapped by corresponding GPM overpasses for (A) Il Monte, (B) Serano, and (C) Lauro sites. The gray area represents the Ku-band swath, and the black area represents the Ka-band swath, while the dots indicate the center of each footprint. The red plus sign indicates the location of the GR.

- Used with permission from D'Adderio, L. P., Vulpiani, G., Porcù, F., Tokay, A., & Meneghini, R. (2018). Comparison of GPM core observatory and ground-based radar retrieval of mass-weighted mean raindrop diameter at midlatitude. *Journal of Hydrometeorology*, 19(10), 1583–1598. <https://doi.org/10.1175/JHM-D-18-0002.1> © American Meteorological Society.

17.5.1 MICROPHYSICAL AND INTEGRAL DSD PARAMETERS ESTIMATION FROM GR DATA

The DSD parameters (i.e., D_m and N_w) are estimated from GR by using a retrieval approach based on a neural network (NN) inversion technique (Vulpiani et al., 2006). They can be also derived through empirical relationships linking them to radar measurements as the horizontal reflectivity (Z_H) and the differential reflectivity (Z_{DR}). This is the standard approach (i.e., derive the reference DSD parameters from empirical relationships) that is applied to the data from GPM VN (Gatlin et al., 2020; Petersen et al., 2020; Tokay et al., 2020). As preliminary sensitivity analysis, the two approaches mentioned earlier (i.e., the NN and the empirical relationships approach) have been compared to test the reliability of the DSD parameters estimation. It has to be highlighted that additional different approaches such as the Bayesian or variational approach (Cao et al., 2010, 2013) are present in literature and could be considered to estimate the DSD parameters.

17.5.2 THE NEURAL NETWORK APPROACH

An artificial NN can be considered a nonlinear parameterized mapping from an input x to an output $y = \text{NN}(x; w; M)$, where w is the vector of parameters (weights and biases) relating the input x to the output y , while the functional form of the mapping (i.e., the architecture of the net) is denoted as M . The nonlinear neuron model, rep-

representing the basic processing unit, is composed by (1) a set of synapses, each of which is characterized by a weight; (2) an adder for summing the input signals, weighted by the respective synapses of the neuron; and (3) an activation function u for limiting the amplitude of the output of a neuron. In mathematical terms a given neuron output y_k can be written as $y_k = \varphi(a_k)$ with $a_k = \sum_{j=1}^p w_{k,j} x_j + b_k$ where x_j is the input to the j th synapse, $w_{k,j}$ is the synaptic weight, $b_k = w_{k,0} x_0$ (with $x_0=1$) is the bias, and φ is the activation function. The NN considered here is a multilayer perceptron architecture with back-propagation learning algorithm. It was originally proposed by Vulpiani et al. (2006) for S-band, where the retrieval uncertainties were addressed with respect to a simulated and real dataset and adapted here for C-band radar measurements to estimate the parameters of the assumed normalized Gamma distribution (i.e., the intercept parameter N_w , the median diameter D_0 , and the shape parameter μ). Variables D_0 and N_w are independently estimated using distinct NNs, namely, NN_{N_w} and NN_{D_0} , respectively, with three inputs (i.e., Z , Z_{DR} , K_{DP}). The shape parameter μ is estimated from Z_{DR} and from the retrieved values of D_0 [as suggested in Brandes et al. (2002)] using a two-input neural network NN_μ . Then, D_m is computed from D_0 and μ , that is, $D_m = D_0 \frac{4+\mu}{3.67+\mu}$. Once that D_m , N_w , and μ are estimated, the rainfall rate is calculated by applying the Gamma distribution to the DSD represented by the three parameters. We remark that the effects on the DSD parameters of considering a truncated Gamma distribution become more significant decreasing the maximum drop diameter (Adirosi et al., 2015). The NN architecture and regularization parameters were determined according to a heuristic monitoring of the generalization capability on test data, the root-mean-square error (RMSE) having been used as metric. According to what was suggested in Aires et al. (2002), it was found that the one-hidden-layer configuration improves the generalization capability of the NNs. The number of nodes in the hidden layer was fixed to 6 for NN_{D_0} and NN_{N_w} , whereas it was set to 12 for NN_μ .

17.5.3 THE EMPIRICAL RELATIONSHIPS APPROACH

The two DSD parameters considered here can be expressed as a function of radar variables. In particular, D_m , which is the ratio of the fourth to the third moment of the DSD, is expressed as a function of the Z_{DR} through a third-degree polynomial fit:

$$D_m = a \cdot Z_{DR}^3 + b \cdot Z_{DR}^2 + c \cdot Z_{DR} + d \quad (17.1)$$

where D_m is in millimeters and Z_{DR} (dB) is the ratio of the radar reflectivity at horizontal (Z_H) and vertical (Z_V) polarizations. On the other hand, N_w is related to Z_H and D_m through the following relationship:

$$N_w = \alpha \cdot Z_H \cdot D_m^\beta \quad (17.2)$$

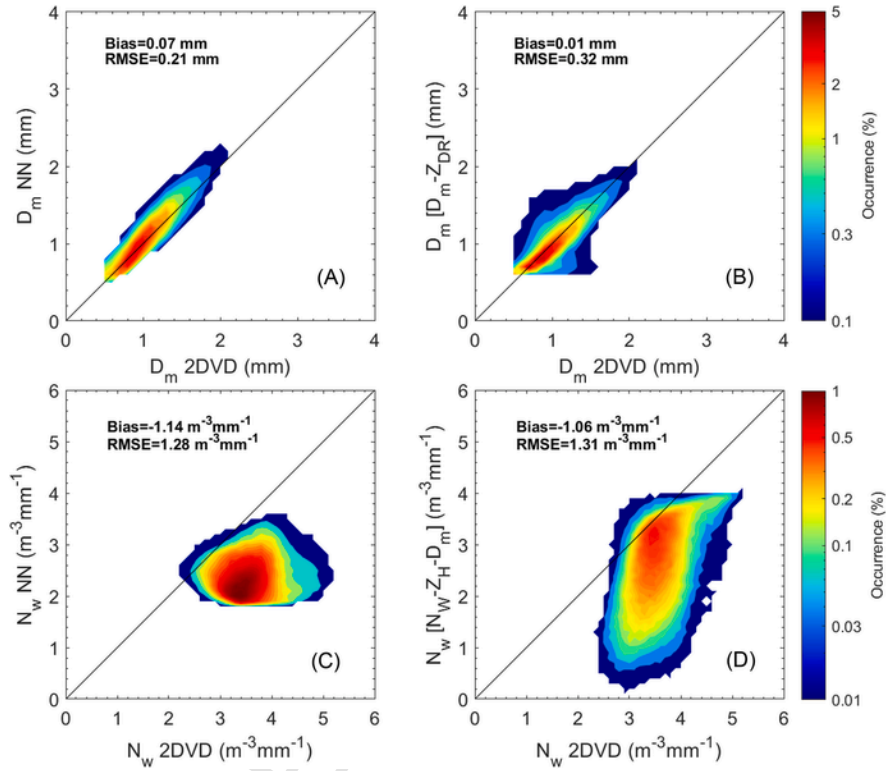
where N_w is expressed in $\text{m}^{-3} \text{mm}^{-1}$. While D_m is directly calculated from the DSD measurements, Z_{DR} is obtained by simulating Z_H and Z_V at the operating radar frequency (i.e., C-band for the Italian DPC GRs) through the T-matrix scattering model (Mishchenko, 2000). The T-matrix scattering model assumes the axis ratio of the oblate spheroid as input and in this study the Brandes et al. (2002) model has been used, even if different models given in the literature (Andsager et al., 1999; Beard & Chuang, 1987; Thurai et al., 2007; Thurai & Bringi, 2005) have been tested resulting in very similar D_m - Z_{DR} relationships. The 2DVD data collected during the GPM GV program (i.e. the data collected during the field campaigns and the permanent measurement fields reported in Section 17.2.3) have been used to derive the D_m - Z_{DR} relationship by applying the sequential intensity filtering technique (SIFT; Lee & Zawadzki, 2005). The SIFT method calculates the mean values of the retrieved variable D_m for each prescribed bin of the observed variable Z_{DR} . For each Z_{DR} bin, 0.1-dB width, the mean value is also calculated as long as the sample size is above a certain threshold that we set to 10 samples. The linear least squares method is then applied to the D_m - Z_{DR} pairs obtaining the coefficients a , b , c , and d of Eq. (17.1). The same dataset and the same procedure have been applied to derive the coefficients α and β from Eq. (17.2). The coefficients derived both for D_m - Z_{DR} and N_w - Z_H - D_m relationships are reported in Table 17.5.

17.5.4 A PRELIMINARY ANALYSIS ON THE DERIVATION OF THE DSD PARAMETERS

To investigate the differences deriving from employing the NN or the empirical relationship approach to derive the DSD parameters (i.e., D_m and N_w), both methodologies have been applied both to 2DVD data and GR data. From the 2DVD data, Z_{DR} at C-band has been simulated to compute D_m through Eq. (17.1): the derived D_m is then compared with D_m calculated from DSD data (i.e., as ratio between the fourth and the third moment of DSD). The same procedure has been done to derive N_w . On the other hand, the radar variables used in input to the NN have been simulated to derive D_m and N_w by using this approach. The result of the comparison is shown in Fig. 17.12. When the NN approach is applied to the 2DVD data, the re-

Table 17.5 Coefficients a , b , c , and d for D_m - Z_{DR} relationship and coefficients α and β for N_w - Z_H - D_m relationship derived from 2-D video disdrometer data.

$D_m = a \cdot Z_{DR}^3 + b \cdot Z_{DR}^2 + c \cdot Z_{DR} + d$		$N_w = \alpha \cdot Z_H \cdot D_m^\beta$	
a	0.0138	α	35.3
b	-0.1696	β	-7.2
c	1.1592		
d	0.7215		

**FIGURE 17.12**

2-D density plot of the comparison between D_m measured by 2DVD and D_m estimated by applying the (A) NN approach and (B) $D_m - Z_{DR}$ relationship to the 2DVD data and between N_w measured by 2DVD and N_w estimated by applying the (C) NN approach and (D) $N_w - Z_H - D_m$ relationship to the 2DVD data. The normalization is done with respect to the total number of samples. 2DVD, 2-D video disdrometer; NN, neural network.

sulting D_m is highly correlated to the measured D_m (Fig. 17.12A), with a slightly trend to overestimate the measured D_m as also shown by low positive bias value (0.07 mm). For a given 2DVD-based D_m the interval $D_m(NN) \pm 0.2$ mm contains a fraction of samples ranging between 87% and 58% at 1 and 2 mm, respectively. If the interval $D_m(NN) \pm 0.3$ mm is considered, the fraction increases to 94% and 77%, respectively. The D_m derived when the $D_m - Z_{DR}$ relationship is applied to 2DVD data shows a very good agreement with the reference values (bias = 0.01 mm) but a slightly larger spread (Fig. 17.12B). In this case the range of occurrence is lower both in the $D_m \pm 0.2$ and $D_m \pm 0.3$ mm interval. The low RMSE values highlight the high reliability of both methodologies in estimating D_m with a minimal better performance of NN approach. The situation is quite different for N_w . Both methodologies show more marked issues in correctly estimating this parameter (Fig. 17.12C

and D). While the NN approach provides logarithmic values of N_w mainly between 2 and $3.5 \text{ m}^{-3} \text{ mm}^{-1}$, the empirical relationship approach provides values over a wider range (between 0.5 and $\text{m}^{-3} \text{ mm}^{-1}$) but both showing a bad agreement with the reference values.

Both Eqs. (17.1) and (17.2) have been applied to the GR data (i.e., Z_{DR} and Z_H measured by GR) and the resulting D_m and N_w have been compared with those provided by NN (Fig. 17.13). The results reflect what shown in Fig. 17.12, with a very good and quite bad agreement for D_m and N_w , respectively.

17.5.5 DPR AND DPR–GMI PERFORMANCE

This paragraph shows the results obtained when the microphysical and integral DSD parameters (i.e., D_m , N_w , and RR) provided by GPM products are compared with those provided by GR. We considered four products, two based on DPR only (i.e., DPR) and two based on combination of DPR and GMI information (i.e., DPR–GMI). For each category the products provided on the Ms (i.e., taking into account the measurements at both Ka- and Ku-band) and on the NS (i.e., taking into account the measurements at Ku-band only) are considered. We recall one more time, that even if the data analyzed in this chapter provided for products at HS (i.e., taking into account the measurements at Ku-band only exclusively for DPR), we decided to not use these data. The choice is based on the fact that the scan mode of DPR has been changed on May 18, 2018 and the high-sensitivity data will be not available any more. Before proceeding to comparisons of the DSD parameters, we first consider comparisons of reflectivities measured by the spaceborne and GRs, considering that while the GPM radars work at Ka- and Ku-band, the GRs work at C band. Since the Ka-band reflectivity is provided only for DPR Ms, while the Ku-

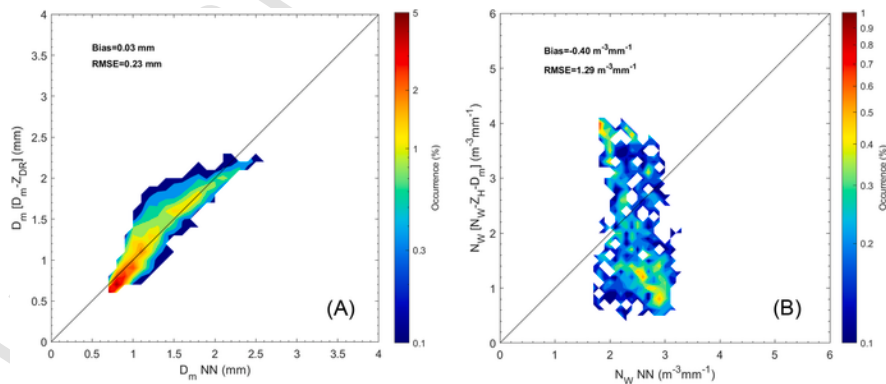


FIGURE 17.13

2-D density plot of the comparison between the (A) D_m and (B) N_w estimated by NN and empirical relationships when the two approaches are applied to GR data. The normalization is done with respect to the total number of samples. GR, Ground radar; NN, neural network.

band reflectivity is provided for both DPR Ms and DPR NS, we decided to show only the comparison between Ku- and C-band reflectivity. Furthermore, because of the negligible difference between the DF- and SF-based (i.e., Ku-only based) products, as also shown in Section 17.4, we decided to show only the comparison for the DPR products (i.e., the DF-based products), while the performances quantified by statistical scores will be reported for each product in Table 17.6. Fig. 17.14 shows the 2-D density plot (normalized with the total number of samples) between DPR Z_{Ku} and GR Z_C for stratiform (top row) and convective (bottom row) precipitation over land (left column) and over sea (right column). The “other” precipitation type has too few samples for all scan and surface types and is not considered; the same is true for the coast and it is not considered as well. The agreement is quite good, even if especially over land DPR Z_{Ku} overestimates GR Z_C both for stratiform and convective precipitations (Fig. 17.14A and C, respectively). For precipitation over sea the agreement is slightly better for stratiform than convective precipitation with most of the points on the one-to-one line, especially at low and medium Z values (Fig. 17.14B), while the overestimation is still evident for convective precipitation (Fig. 17.14D). As it could be expected, the distribution moves toward higher reflectivities during convective precipitation with respect to the stratiform ones.

Both the DPR- and DPR-GMI-estimated D_m , N_w , and R have been compared with the reference GR-based D_m , N_w , and RR . As highlighted earlier, since the difference between the four products considered (i.e., DPR Ms, DPR NS, DPR-GMI Ms, and DPR-GMI NS) is quite limited, those (four products) are shown only the 2-D density plot of DPR Ms, which is the DF-based algorithm-based on DPR measurements only. Fig. 17.15 shows the 2-D density plot for D_m . The agreement is quite good for stratiform precipitation (Fig. 17.15A and B) where most of the D_m values are distributed around 1 mm both for GR and DPR. While, over land, there is a slight overestimation for larger D_m values (Fig. 17.15A), over sea, there is an underestimation at medium to large D_m values (Fig. 17.15B). During convective precipitation the retrieval of D_m evidences more difficulties leading to an overestimation both over land (Fig. 17.15C) and over sea (Fig. 17.15D). Furthermore, the lower number of samples collected during this type of precipitation does not allow a clear trend in the distribution. The results shown for D_m are in good agreement with the findings of Gatlin et al. (2020), especially for stratiform precipitation over land (it has to take into account that they labeled the footprints only with respect to the precipitation type but not with respect to the surface type as done in this work). The spread of the distribution is wider if compared with their results, depending also on the different size of the available datasets.

The retrieval of N_w is even worse (Fig. 17.16). The logarithmic values of N_w estimated by DPR is enclosed in a very limited interval ranging between 2.6 and $3.6 \text{ m}^{-3} \text{ mm}^{-1}$ as also already discussed in Section 17.4. This is true especially for stratiform precipitation resulting in a clear overestimation of N_w (Fig. 17.16A and B), while a wider range of values are provided during convective precipitation resulting in a slightly better agreement with GR-based N_w (Fig. 17.16C and D).

A

sensitivity

Table 17.6 Sample size and statistics for drop size distribution parameters estimation of both dual-frequency precipitation radar (DPR) and DPR–Global Precipitation Measurement microwave imager (GMI) algorithm.

			DPR versus GR				DPR–GMI versus GR			
			<i>Land</i>		<i>Sea</i>		<i>Land</i>		<i>Sea</i>	
			Ms	NS	Ms	NS	Ms	NS	Ms	NS
<i>Z</i>	Sample size	Stratiform	1297	1686	934	1123	631	722	556	596
		Convective	510	683	352	411	334	433	243	284
	ME	Stratiform	5.09	5.27	2.39	2.84	/	/	/	/
		Convective	5.24	6.20	4.68	5.54	/	/	/	/
	FSE	Stratiform	31.2	32.8	18.8	22.0	/	/	/	/
		Convective	26.2	27.9	25.4	28.0	/	/	/	/
	CC	Stratiform	0.78	0.74	0.87	0.84	/	/	/	/
		Convective	0.76	0.79	0.70	0.70	/	/	/	/
<i>D_m</i>	ME	Stratiform	0.26	0.26	0.04	0.03	0.12	0.10	−0.22	−0.21
		Convective	0.62	0.98	0.34	0.37	0.29	0.35	0.00	0.06
	FSE	Stratiform	39.3	34.8	28.9	22.7	38.5	36.6	25.9	27.9
		Convective	53.9	91.0	43.9	43.8	36.6	40.4	27.2	27.2
	CC	Stratiform	0.54	0.56	0.65	0.77	0.51	0.52	0.79	0.73
		Convective	0.61	0.60	0.42	0.59	0.57	0.55	0.62	0.64
	ME	Stratiform	0.72	0.71	0.62	0.68	0.94	0.98	1.03	1.09
		Convective								

Table 17.6 (Continued)

			DPR versus GR				DPR–GMI versus GR			
			<i>Land</i>		<i>Sea</i>		<i>Land</i>		<i>Sea</i>	
			Ms	NS	Ms	NS	Ms	NS	Ms	NS
N_w	FSE	Convective	0.34	0.10	0.57	0.64	0.78	0.80	1.17	1.18
		Stratiform	39.3	33.7	33.1	31.2	46.7	47.5	44.0	46.0
		Convective	32.6	33.6	35.2	36.3	37.2	38.0	49.1	49.6
	CC	Stratiform	−0.13	0.22	0.01	0.27	−0.53	−0.43	−0.23	−0.10
		Convective	−0.11	−0.32	0.10	−0.15	−0.24	−0.21	−0.13	−0.03
	ME	Stratiform	2.30	2.95	−0.13	1.01	2.71	3.44	1.11	2.10
R	FSE	Convective	3.61	4.67	4.19	3.82	7.47	10.10	9.79	9.63
		Stratiform	294.6	343.0	146.8	178.4	428.8	520.8	174.6	257.2
		Convective	234.1	258.7	166.4	176.7	219.8	154.3	173.9	169.3
	CC	Stratiform	0.39	0.50	0.47	0.43	0.26	0.34	0.38	0.58
		Convective	0.42	0.45	0.67	0.67	0.47	0.48	0.81	0.79

For each indicator and for each type of precipitation (stratiform/convective) and surface (land/sea). CC, Correlation coefficient; FSE, fractional standard error; GR, ground radar; ME, mean error; Ms, matched scan; NS, normal scan.

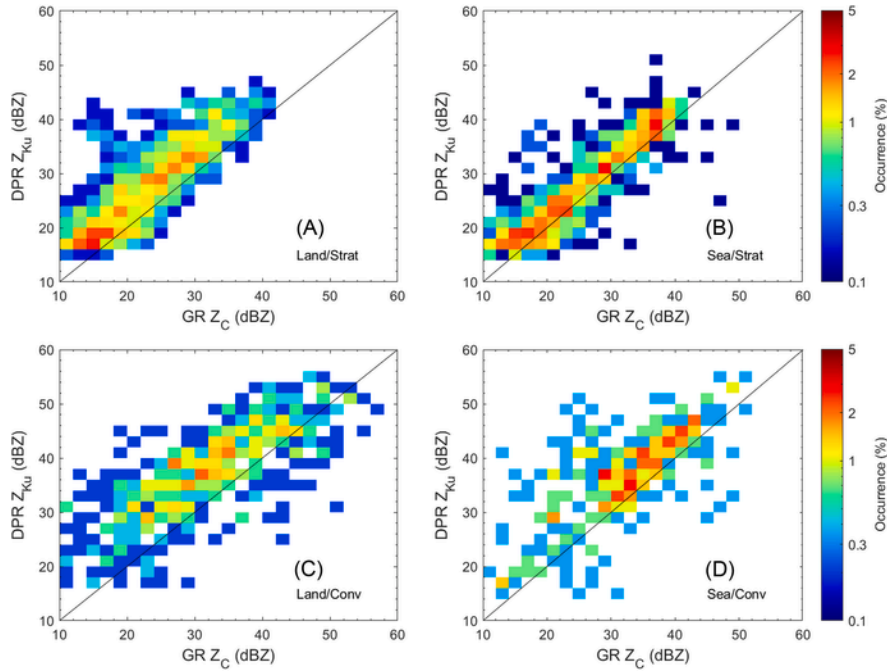


FIGURE 17.14

2-D density plot of the comparison between reflectivity measured by GR at C-band (corrected by ground clutter, attenuation, etc.) and reflectivity measured by GPM radar at Ku-band (corrected by ground clutter, attenuation, etc.) for each combination of surface (land/sea) and precipitation (stratiform/convective) type. The normalization is done with respect to the total number of samples. *GPM*, Global Precipitation Measurement; *GR*, ground radar.

test has been conducted by comparing N_w estimated by applying Eq. (17.2) to the GR data, but the results do not show any improvement. In addition, the results are not so different if the other products (i.e., DPR NS, DPR-GMI-Ms, or DPR-GMI NS) were considered. Although the agreement with the results shown in Gatlin et al. (2020) is quite good for D_m , the agreement for N_w is markedly worse. They found a quite good agreement for stratiform precipitation and an underestimation of N_w for convective precipitation by analyzing the DPR outputs; a worsening of the results are obtained when they analyze the DPR-GMI outputs.

The R shows a similar behavior regardless of the surface and the precipitation type with a general overestimation more marked for light-to-moderate (i.e., between 0.1 and 3 mm h⁻¹ about) precipitation intensity (Fig. 17.17). The agreement increases moving toward heavier R up to an underestimation for stratiform precipitation over sea (Fig. 17.17B). On the other hand, the overestimation of light-to-moderate R is more marked during convective than stratiform precipitation. The results go in the opposite direction with respect to the results obtained in other works

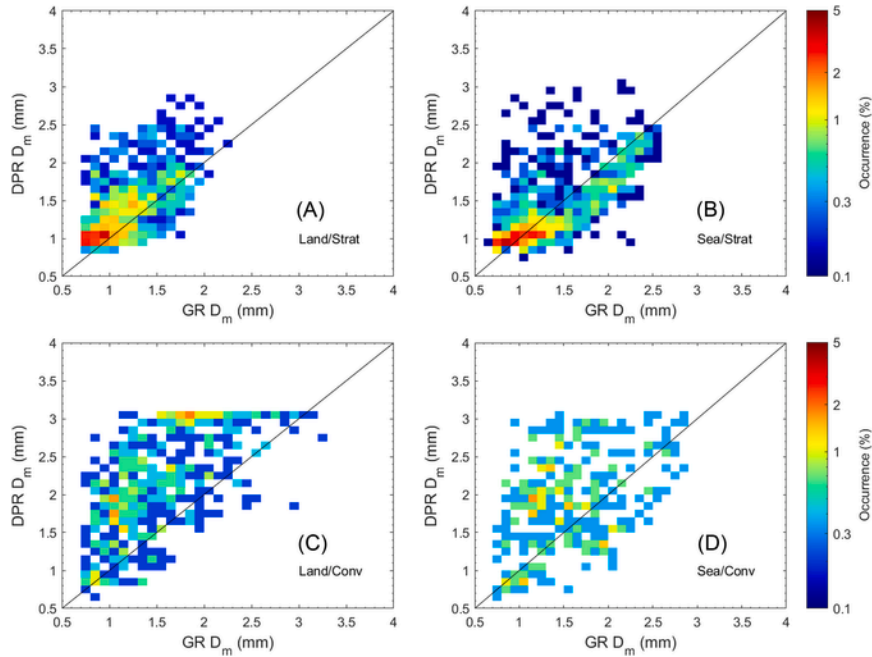
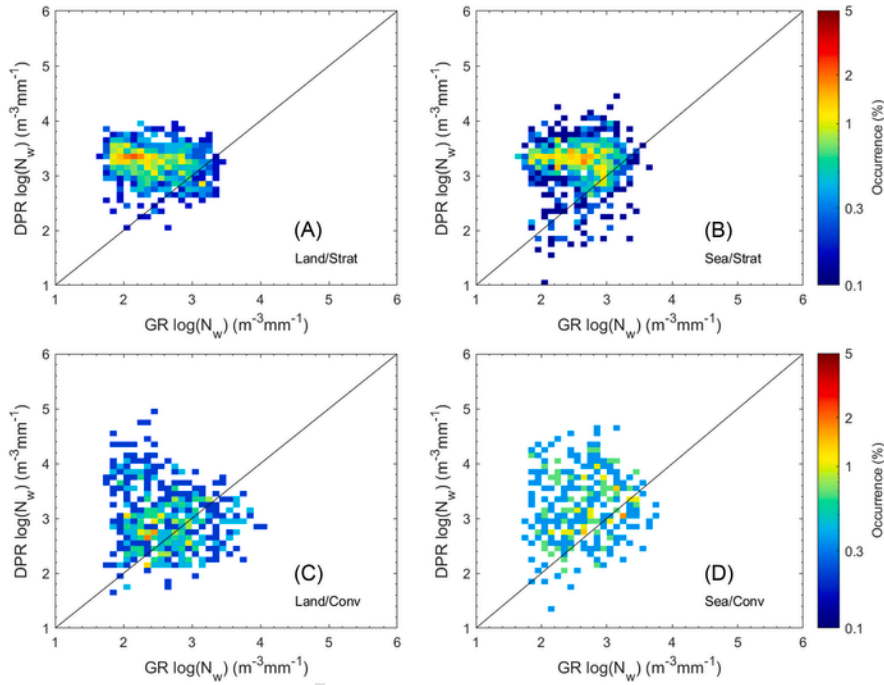


FIGURE 17.15

2-D density plot of the comparison between D_m estimated by GR and D_m estimated by DPR Ms (DF-based) for each combination of surface (land/sea) and precipitation (stratiform/convective) type. The normalization is done with respect to the total number of samples. *DF*, Dual-frequency; *DPR*, dual-frequency precipitation radar; *GR*, ground radar; *Ms*, matched scan.

(Petracca et al., 2018; Speirs et al., 2017; Watters et al., 2018), which found a general underestimation of the DPR-based R estimates, if compared to the measured or estimated R from rain gauges or GR network. It has to be highlighted that they analyzed a different GR products (i.e., the national-level rainfall product derived by combining all the available radar data) with respect to the one considered in this study that is derived by every single radar. Furthermore, they validated the outputs of different DPR algorithm version [namely, Petracca et al. (2018) and Speirs et al. (2017) used the DPR V04 algorithm, while Watters et al. (2018) used the DPR and DPR-GMI V05, respectively]. This is an aspect that could affect the result of the validation studies since two different DPR algorithm versions could significantly differ to each other.

The performances of both DPR and DPR-GMI based products are quantified through calculating statistical scores. Table 17.6 presents the performances in estimating the DSD parameters in terms of mean error (ME), fractional standard error (FSE), and Pearson correlation coefficient (CC) for DPR and DPR-GMI products, over land and over sea, and for each precipitation and scan type. In addition, the

**FIGURE 17.16**

2-D density plot of the comparison between N_w estimated by GR and N_w estimated by DPR Ms (DF-based) for each combination of surface (land/sea) and precipitation (stratiform/convective) type. The normalization is done with respect to the total number of samples. *DF*, Dual-frequency; *DPR*, dual-frequency precipitation radar; *GR*, ground radar; *Ms*, matched scan.

sample size of each category is also reported. To provide a complete overview of satellite products, the statistical scores are calculated also considering the comparison between Z_{Ku} and Z_C . It is worth noting that even if the DPR–GMI provides Z_{Ku} variable as standard output, it is the same of DPR and, for this reason, the statistical scores are shown only in the DPR section of Table 17.6. The ME is calculated as the mean of the difference between the DSD parameters estimated by DPR/DPR–GMI and by GR, while the FSE (expressed in percentage values) is computed as the ratio between the root mean square error (Nurmi, 2003) and the average of the observations at the ground. As general comment, the ME is almost always positive regardless the surface and precipitation type as well as the scan type (i.e., Ms or NS), indicating a general overestimation of the considered parameters by the satellite products. In particular, Z ME is higher over land than over sea and during convective than stratiform precipitation reaching values as high as 6.20 dBZ at NS. It has to be highlighted that in this case the ME has been calculated between reflectivities working at different frequencies and this aspect could affect the results. The

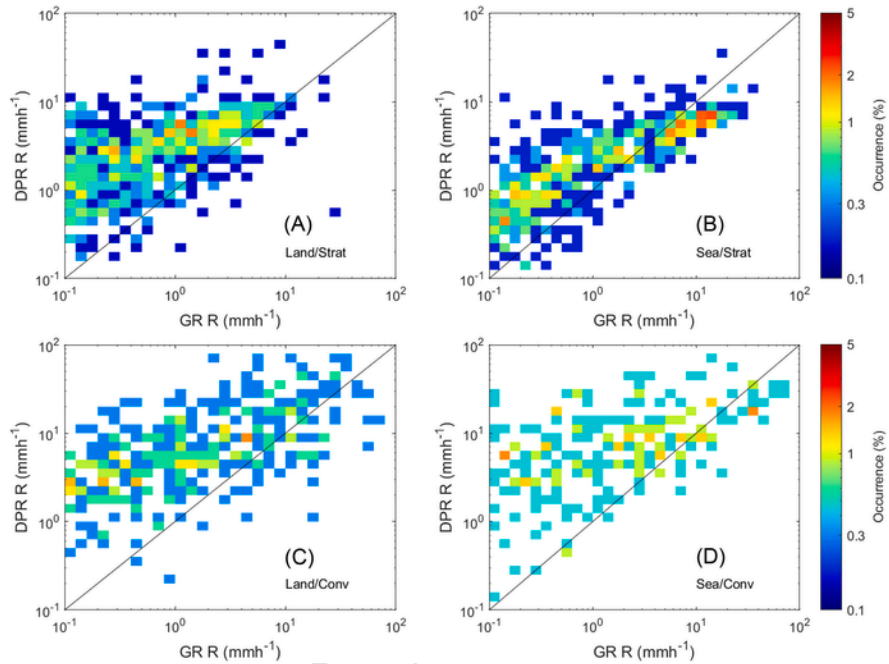


FIGURE 17.17

2-D density plot of the comparison between R estimated by GR and DPR Ms (DF-based) for each combination of surface (land/sea) and precipitation (stratiform/convective) type. The normalization is done with respect to the total number of samples. *DF*, Dual-frequency; *DPR*, dual-frequency precipitation radar; *GR*, ground radar; *Ms*, matched scan.

D_m ME presents the same characteristics of Z ME, with better performances over sea (0.03 mm) than over land (0.26 mm) for DPR products during stratiform precipitation. Its value markedly increases during convective precipitation reaching almost 1 mm for DPR NS product. The DPR–GMI product has better performances over land, both for stratiform and convective precipitations, but worse performances over sea limited to the stratiform precipitation when it reaches negative values around -0.22 mm. The *Ms* outperforms the *NS* both for DPR and DPR–GMI during convective precipitation, while a negligible difference is obtained for stratiform precipitation. The ME values markedly worsening for N_w , as it could be expected from the analysis of 2-D density plot in Fig. 17.16. In this case, better performances are obtained during convective than stratiform precipitation both over land and over sea (except that for DPR–GMI products over sea). We recall that for N_w , the ME is calculated as the difference between the logarithmic values of this parameter and values around $1 \text{ m}^{-3} \text{ mm}^{-1}$ as obtained by both *Ms* and *NS* of DPR–GMI indicate one order of magnitude between the satellite and the ground reference estimation. For RR , the ME shows really different values between stratiform and

convective precipitations with better performances for the latter precipitation type. The worsening of ME values is particularly evident for DPR–GMI product reaching values as high as 10.1 mm h^{-1} with respect to ME values not exceeding 3.5 mm h^{-1} during stratiform precipitation. Again, the performances are better over sea than over land, and for Ms than NS both for DPR and DPR–GMI. The Z FSE presents values ranging between 18% and 32% about, highlighting the good agreement between the satellite and the ground measurements. Its values are lower during convective (stratiform) precipitation over land (sea), while the performances over sea are always better than over land with Ms generally outperforming NS. For D_m , FSE is generally lower during stratiform (the values range between 22% and 39%) than convective (the values range between 27% and 91%) precipitation, while the comparison between land and sea evidences better performances over sea. The Ms outperforms NS during convective precipitation but the opposite is true in the most of the cases during stratiform precipitation both for DPR and DPR–GMI products. Although the agreement between N_w estimated by satellite- and ground-based products was bad, the FSE shows quite low values ranging between 32% and 49% considering all surface, precipitation, and scan type combinations. In particular, over land FSE is lower during convective precipitation, while it is lower during stratiform precipitation over sea. The quite low FSE values can be explained by the limited range of values of N_w being FSE score very sensitive to high differences for the considered parameter. The R FSE is never low than of 176% with peak as high as 520% for DPR–GMI NS over land during stratiform precipitation. The higher FSE during stratiform than convective precipitation could be explained by the overestimation of satellite estimated parameter at low R (Fig. 17.17). At higher R values mainly occurring during convective precipitation, the agreement between DPR/DPR–GMI and GR improves and this reflects in lower FSE values. Finally, the CC is quite high for Z, ranging between 0.70 and 0.87 with better performances for stratiform than convective precipitation. For D_m the CC over land is higher during convective precipitation, while over sea it is higher during stratiform precipitation both for DPR and DPR–GMI products. Contrary to the other statistical scores, the D_m CC does not show a clear trend indicating a better performance of Ms with respect to NS or vice versa. The N_w CC assumes negative values for most of the cases deriving from the poor agreement already discussed for this parameter. The R CC is generally higher during convective precipitation reaching values around 0.80 over sea for DPR–GMI. As for the other scores, it is generally higher over sea than over land, while the occurrence of better performance for Ms than NS is equivalent to the occurrence of better performance of NS with respect to Ms. The statistical scores discussed here are calculated over a significant number of samples (i.e., DPR footprints) ranging between about 3000 samples of DPR Ms to about 3900 samples of DPR NS, while a lower number of samples are collected by DPR–GMI.

A more detailed analysis regarding the reliability of the GPM products is addressed by considering the distribution of the error of the single measure through the percentage error (PE), defined as:

$$PE_i = \frac{Sat_i - GR_i}{GR_i} \cdot 100 \quad (17.3)$$

where *Sat* refers to DSD parameters estimated by DPR or DPR–GMI algorithm and *GR* refers to DSD parameters estimated by GR. Fig. 17.18 reports the distribution of D_m PE as function of both surface and precipitation type (different color and line style, respectively) and as a function of *Ms* and *NS* both for DPR (top row) and DPR–GMI (bottom row). Namely, Fig. 17.18A refers to DPR *Ms*, Fig. 17.18B refers to DPR *NS*, Fig. 17.18C refers to DPR–GMI *Ms*, and Fig. 17.18D refers to DPR–GMI *NS*. All the four panel show very similar characteristics. The negative D_m PE reach (in absolute value) lower values than positive one (–50% with respect to +150% or more). For stratiform precipitation over sea (*solid red lines*), the distributions of PE peak between –20% (for DPR products) and –30% (for DPR–GMI), with a narrower spread for DPR–GMI. The distribution of D_m PE for stratiform precipitation over land is generally wider and shifted toward larger (positive) values

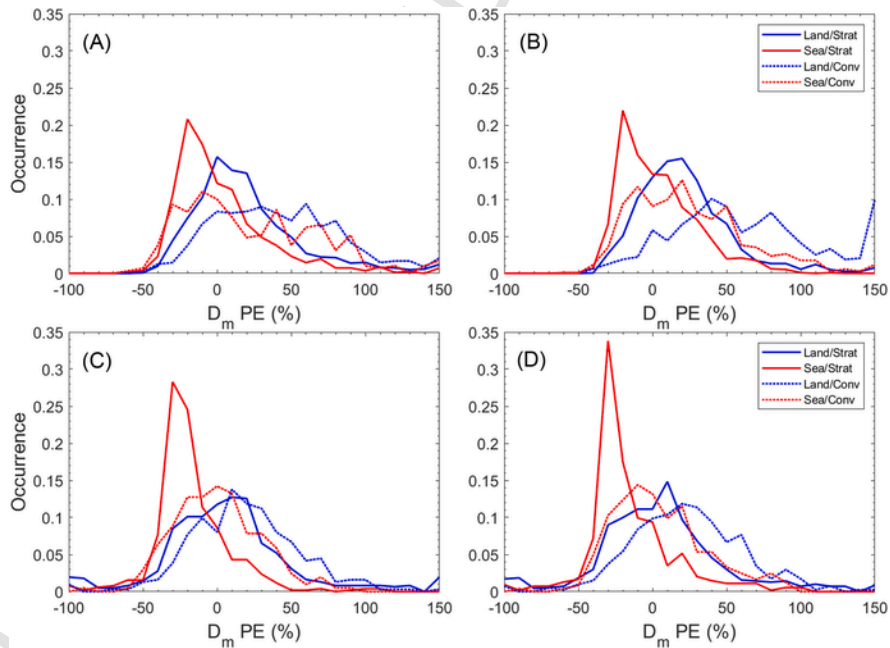


FIGURE 17.18

Distribution of D_m PE for the DPR (top row) and DPR–GMI (bottom row) algorithm. The left column refers to *Ms*, while the right column to *NS*. The blue and red lines refer to land and sea classification, respectively, while the solid and dashed lines refer to stratiform and convective precipitations, respectively. *DPR*, Dual-frequency precipitation radar; *GMI*, GPM microwave imager; *Ms*, matched scan; *NS*, normal scan; *PE*, percentage error.

peaking between 0% and 20% about. For convective precipitation the spread of the distribution for DPR–GMI is generally smaller than DPR, which shows the peak of the distribution at higher D_m PE values. Furthermore, the peak for convective precipitation over sea is more centered on 0% with respect to the convective precipitation over land for both DPR and DPR–GMI.

Fig. 17.19 is the same as Fig. 17.18 but refers to N_w PE. At a first look, it is possible to note that the distributions of N_w PE do not show any marked difference as a function of surface and precipitation type. This is mainly due to the limited range of N_w values estimated by DPR and DPR–GMI algorithm. At the same time the distribution of N_w PE for DPR–GMI is moved toward larger and almost always positive values (Fig. 17.19C and D) if compared to DPR (Fig. 17.19A and B) indicating a general constant and more marked overestimation of N_w .

The distribution of R PE does not show a clear trend as for D_m and N_w (Fig. 17.20). Excluding the stratiform precipitation over sea for DPR Ms (Fig. 17.20A), all the other combinations of surface and precipitation type evidence that the peak of distribution is reached for R PE higher than 500%. This behavior is related to the

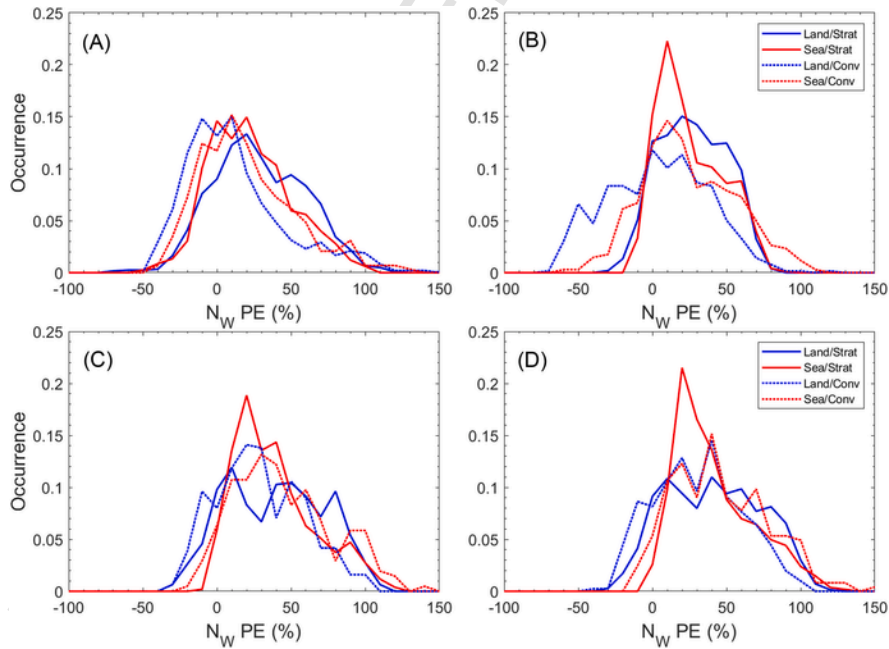
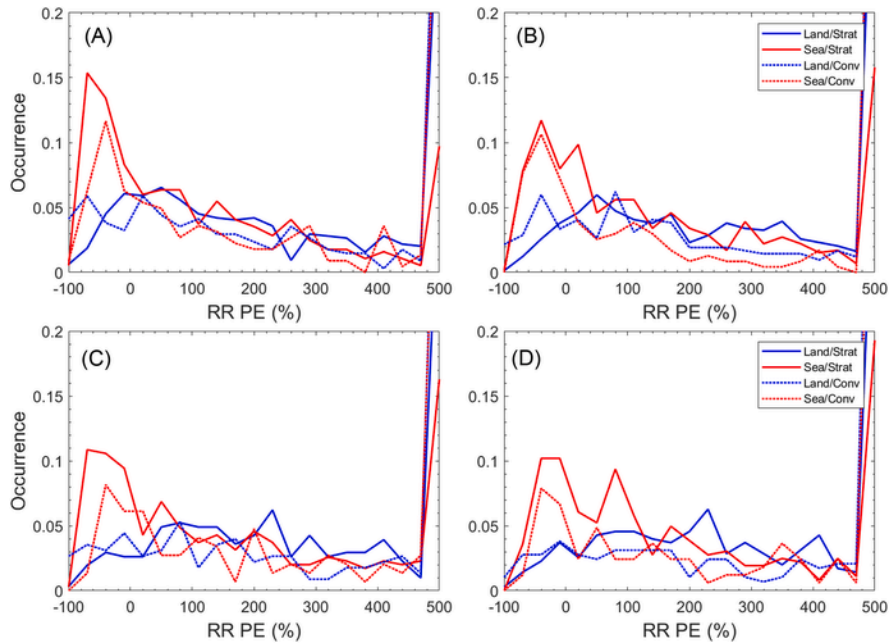


FIGURE 17.19

Distribution of N_w PE for the DPR (top row) and DPR–GMI (bottom row) algorithm. The left column refers to Ms, while the right column to NS. The blue and red lines refer to land and sea classification, respectively, while the solid and dashed lines refer to stratiform and convective precipitations, respectively. *DPR*, Dual-frequency precipitation radar; *GMI*, GPM microwave imager; *Ms*, matched scan; *NS*, normal scan; *PE*, percentage error.

**FIGURE 17.20**

Distribution of R PE for the DPR (top row) and DPR-GMI (bottom row) algorithm. The left column refers to Ms , while the right column to NS . The blue and red lines refer to land and sea classification, respectively, while the solid and dashed lines refer to stratiform and convective precipitations, respectively. *DPR*, Dual-frequency precipitation radar; *GMI*, GPM microwave imager; *Ms*, matched scan; *NS*, normal scan; *PE*, percentage error.

fact that the PE reaches very high values at very low rain rate to decrease moving toward higher rain rate. The secondary peak is located at PE values around -50% for precipitation (both stratiform and convective) over sea, while it moves toward positive PE for precipitation over land, where it is not well defined.

17.5.6 SENSITIVITY ANALYSIS

Some sensitivity analyses have been carried out to further test the reliability of the results and to potentially find reasons for the disagreement between satellite and ground-based estimates of DSD parameters. A matching pair of points is defined as the intersection of the GR and DPR beams. Potential matches range from the first DPR CFB (which depends on the spaceborne radar incidence angle and on the topography and surface characteristics) to the highest level with liquid precipitation (which depends on the characteristics of the precipitation event). The farther the distance from the GR, the larger the volume of the radar resolution cell, regardless the elevation angle. As the volume increases, the variability of the rain structure

within can become significant, leading to a NUBF issue with the GR. It follows that both the distance from the GR and the presence of NUBF within a satellite footprint can play a role in obtaining a better or worse agreement between satellite- and ground-based measurements. In this frame, we investigated the dependence of the PE both on the distance from GR and on the NUBF. Fig. 17.21 shows the trend of mean $PE \pm$ one standard deviation with respect to the distance of the matching point from the GR, sampled in classes of 10-km width, for D_m . The plot reveals a sinusoidal trend for both stratiform (Fig. 17.21A) and convective (Fig. 17.21B) precipitation and for both DPR and DPR–GMI products whether Ms or NS labeled by different colors). In particular, Fig. 17.21A shows a slight increase of mean D_m PE up to 80 km, followed by a decrease and a further increase for distance larger than 120 km from GR. In addition, the mean D_m PE for DPR–GMI (green and black lines) presents values closer to 0% than DPR (blue and red lines) but, at the same time, a greater width of the distribution. Similar considerations are applicable to the convective precipitation, but the increase of D_m PE continues up to 120 km and then decrease for distance from GR larger up to 150 km (Fig. 17.21B). Moreover, DPR shows both larger mean and standard deviation D_m PE with respect to DPR–GMI. The difference between Ms and NS is negligible except that for convective precipitation when DPR Ms outperforms DPR NS. Both stratiform and convective precipitations do not show the highest D_m PE values at the farthest distance from GR but at distances ranging between 50 and 110 km depending on the product and scan type considered.

The results do not appreciably change for N_w . Fig. 17.22 always shows an oscillating trend for N_w PE, even if in a constant increase context. This is true for strati-

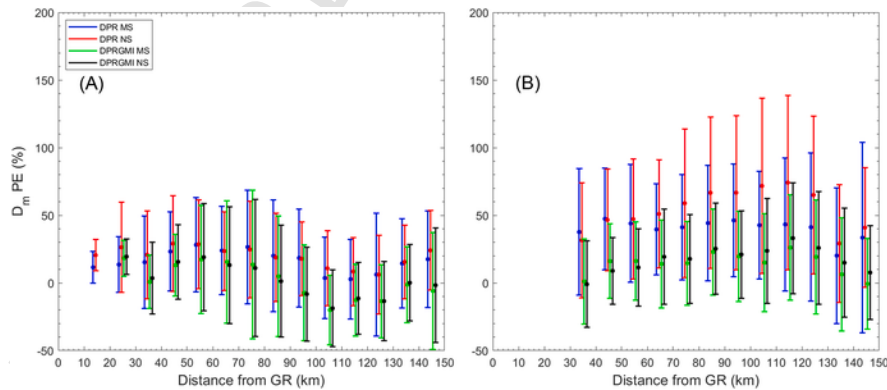


FIGURE 17.21

Mean \pm standard deviation of D_m PE with respect to the distance of the matching point from GR for (A) stratiform and (B) convective precipitation. The line colors are blue for DPR Ms, red for DPR NS, green for DPR–GMI Ms, and black for DPR–GMI NS. *DPR*, Dual-frequency precipitation radar; *GMI*, GPM microwave imager; *GR*, ground radar; *Ms*, matched scan; *NS*, normal scan; *PE*, percentage error.

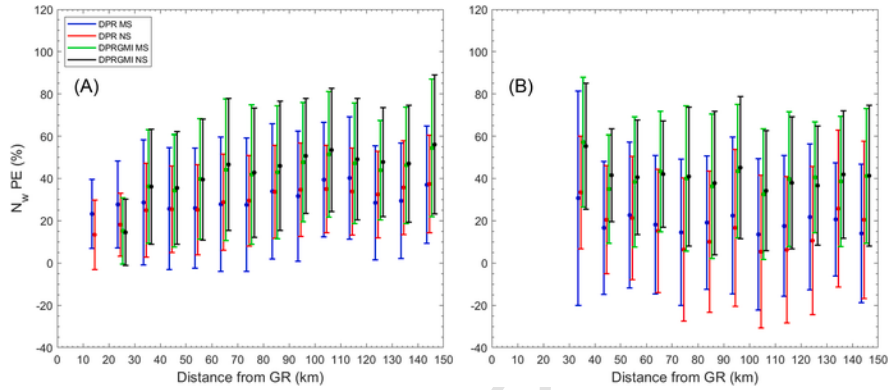


FIGURE 17.22

Mean \pm standard deviation of N_w PE with respect to the distance of the matching point from GR for (A) stratiform and (B) convective precipitation. The line colors are blue for DPR Ms, red for DPR NS, green for DPR-GMI Ms, and black for DPR-GMI NS. *DPR*, Dual-frequency precipitation radar; *GMI*, GPM microwave imager; *GR*, ground radar; *Ms*, matched scan; *NS*, normal scan; *PE*, percentage error.

form precipitation, regardless the GPM product and the scan type (Fig. 17.22A), while the N_w PE values are more constant as a function of GR distance for convective precipitation (Fig. 17.22B). On the other hand, although the width of the distribution for each distance bin is comparable between DPR and DPR-GMI, the latter presents constantly higher mean values of N_w PE. Furthermore, not appreciable differences are obtained between Ms and NS for both DPR and DPR-GMI.

The analysis of R PE evidences marked differences between stratiform and convective precipitations (Fig. 17.23). During stratiform precipitation, R PE shows small variations with respect to the distance from GR, while the width of the distribution can change significantly moving from a distance bin to another (Fig. 17.23A). Generally, Ms outperforms NS for both DPR and DPR-GMI especially at medium-range distance (e.g., between 50 and 90 km). This is the only characteristic also shown by convective precipitation (Fig. 17.23B) that, on average, presents higher mean values of R PE and marked higher standard deviation values of R PE (to preserve a good readability of both parts (A) and (B) the lower and upper y-axis limit has been set to -200% and 1000% , respectively).

The inhomogeneity of the rain structure in space and time can affect the rain measurement at different scales (Tokay et al., 2016; Tokay et al., 2017), resulting in NUBF situations. We took into account this effect considering the different spatial resolutions of the DPR and GR through the comparison process as well as the NUBF is taken into account by the GPM algorithms (Iguchi, 2017). This resolution difference allows us to analyze in more detail the effects of NUBF on the DSD parameters estimation. To analyze the impact of NUBF, two indicators have been considered: the percentage of GR pixels below the minimum detectable signal (10

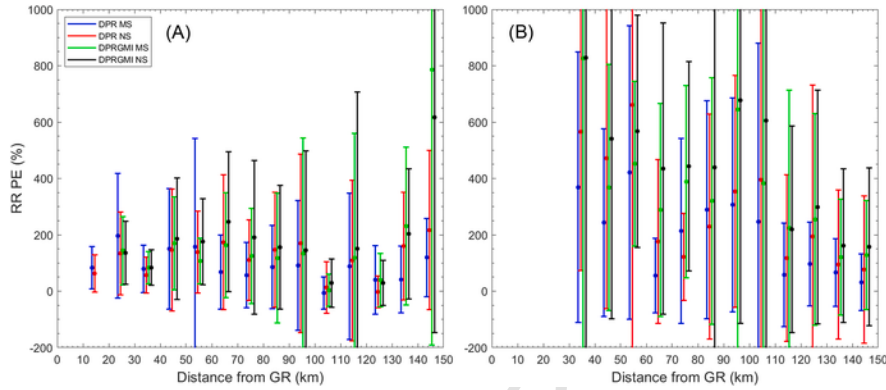


FIGURE 17.23

Mean \pm standard deviation of R PE with respect to the distance of the matching point from GR for (A) stratiform and (B) convective precipitation. The line colors are blue for DPR Ms, red for DPR NS, green for DPR-GMI Ms, and black for DPR-GMI NS. *DPR*, Dual-frequency precipitation radar; *GMI*, GPM microwave imager; *GR*, ground radar; *Ms*, matched scan; *NS*, normal scan; *PE*, percentage error.

dBZ) and the Z_C standard deviation of GR pixels above the minimum detectable signal within a DPR footprint. Fig. 17.24 shows the dependence of D_m PE as function of the two indicators used to quantify the NUBF. The plots that are very similar to each other (i.e., there is no dependence on scan, Ms or NS, and algorithm, DPR or DPR-GMI type) do not show a clear trend, even if some indications can be deducted. An increase of GR pixel below the minimum detectable signal pushes the D_m PE toward higher positive values, while an increase of Z_C standard deviation does not necessarily mean an increase of D_m PE.

If the convective precipitation is considered, any marked difference with respect to the stratiform one is noticeable (Fig. 17.25). Because of the analysis did not produce any significant results for N_w and RR , we decided to not show the related plots.

As final analysis, a very low number of cases reporting a missing value for the considered DSD parameters have been investigated by comparing the reflectivity measured by both DPR (i.e., the signal not corrected for attenuation and ground clutter) and GR. We limited to the DPR Ms since both Ka- and Ku-band measured reflectivity values have been considered. This analysis shows that reflectivity measured at both Ka- and Ku-band for the most of the considered samples is below the DPR minimum detectable signal regardless the surface and precipitation type, while the GR measured low reflectivity values between 10 and 20 dBZ (Fig. 17.26).

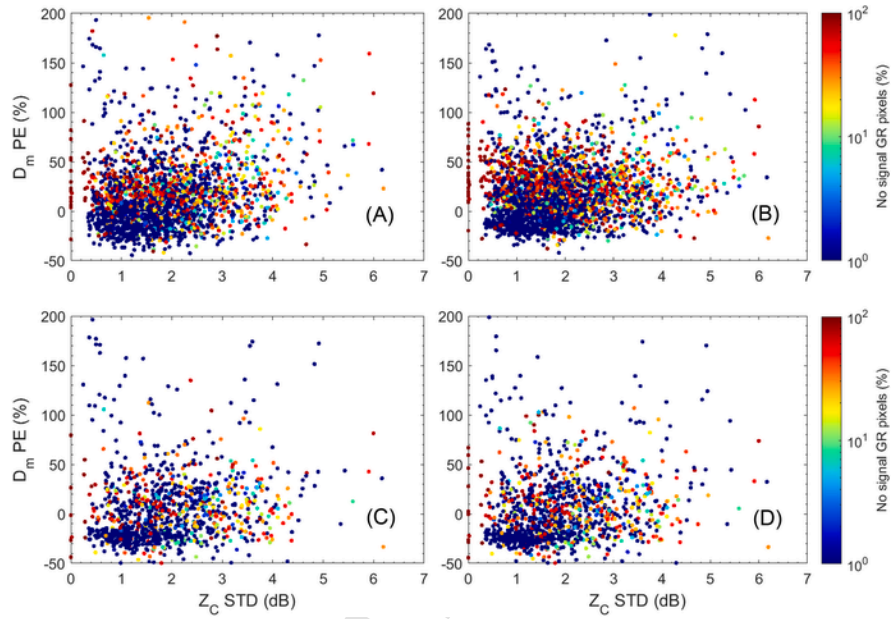


FIGURE 17.24

Dependence of D_m PE with respect to the number of no-rain GR pixels and their standard deviation within a DPR footprint for DPR (A) Ms, (B) NS, and for DPR–GMI (C) Ms and (D) NS for stratiform precipitation. *DPR*, Dual-frequency precipitation radar; *GMI*, GPM microwave imager; *GR*, ground radar; *Ms*, matched scan; *NS*, normal scan; *PE*, percentage error.

17.6 CONCLUSION

The GPM DPR provides the 3-D microphysical structure of precipitation as well as the near-surface precipitation intensity at global scale, thanks to the relationship between radar reflectivity and the physical characteristics of the precipitation. Both SF- and DF-based algorithms have been designed to retrieve DSD parameters, and other bulk properties of precipitation (e.g., precipitation rate, liquid and ice water contents), for each bin in the vertical profile by assuming that the DSD is described by a three-parameter normalized Gamma distribution. The SF- and DF-based algorithms require various assumptions and corrections (i.e., for attenuation and ground clutter) to retrieve precipitation microphysical parameters. In principle, only DF-based algorithms can provide two independent DSD parameters, D_m and N_w , assuming a constant value for the third parameter μ , while the SF-based algorithms need additional constraints to retrieve both D_m and N_w . If, on one hand, the GPM allows to reconstruct the microphysical structure of the precipitation, on the other hand both, microphysical and integral DSD parameters have to be validated to as-

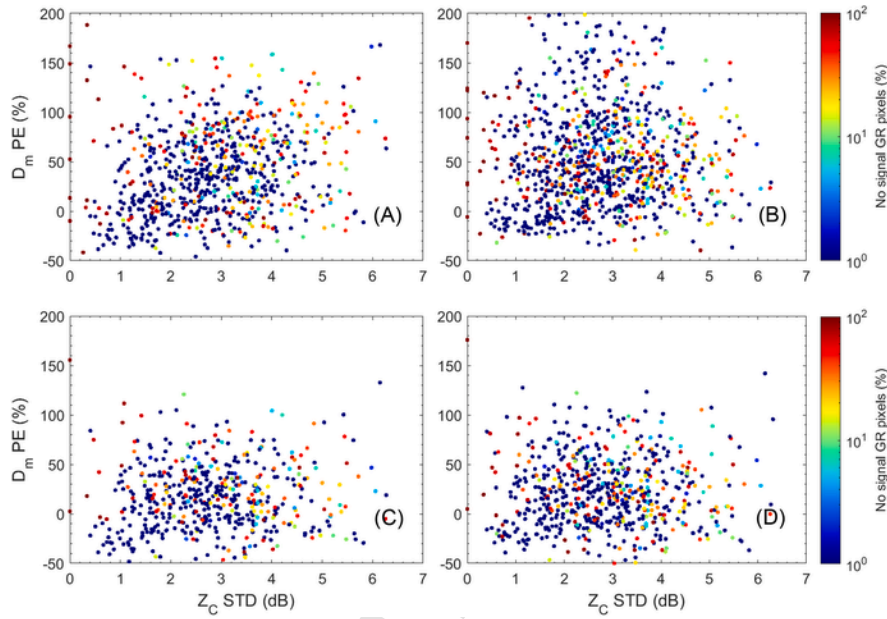


FIGURE 17.25

Dependence of D_m PE with respect to the number of no-rain GR pixels and their standard deviation within a DPR footprint for DPR (A) Ms, (B) NS, and for DPR-GMI (C) Ms and (D) NS for convective precipitation. *DPR*, Dual-frequency precipitation radar; *GMI*, GPM microwave imager; *GR*, ground radar; *Ms*, matched scan; *NS*, normal scan; *PE*, percentage error.

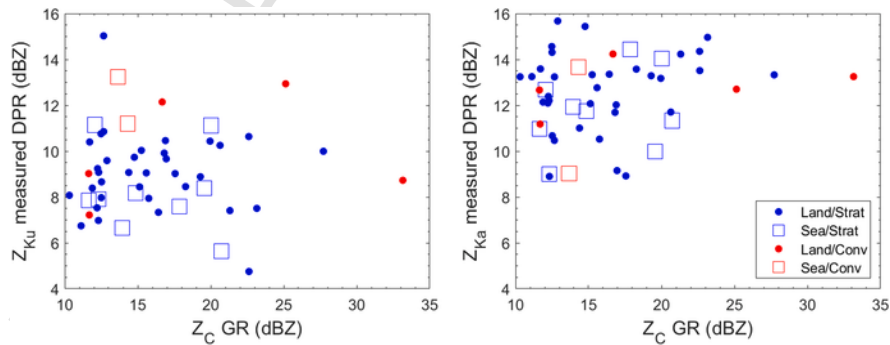


FIGURE 17.26

Reflectivity measured by (A) DPR Z_{Ku} and (B) DPR Z_{Ka} and GR (Z_C) for the cases where the DPR algorithm reported the DSD parameters as missed value. *DPR*, Dual-frequency precipitation radar; *DSD*, drop size distribution; *GR*, ground radar.

sess the reliability of satellite measurements. The validation has two major components: the physical validation, which is conducted to evaluate the assumptions in the DPR algorithms utilizing targeted field campaign datasets; while the direct validation is performed by comparing ground- (e.g., single- and dual-polarized radars, disdrometers, and rain gauge networks) and GPM-based estimates. The GPM GV program posted Level-1 requirements, which include the accuracy of DPR DSD and precipitation rate (Skofronick-Jackson et al., 2017). While GPM DPR products, specifically SF- and DF-based products, are individually validated through direct comparison with the ground-based measurements, there is no study for the cross-comparison of these products to investigate the consistency of their outputs.

The purpose of this chapter is to critically investigate on and assess the consistency of the precipitation structures provided by the different DPR algorithms comparing the SF- (both Ku- and Ka-band) and DF-based estimates (taken as reference). The comparison has been carried out over the Mediterranean area, comparing the products at the NSL and along the vertical profile. The analysis takes into account the difference between surface types (land/sea) and precipitation types (stratiform/convective) as provided by the DPR DF products. The analysis of the precipitation phase shows that the Ku-only precipitation phase output is almost in perfect agreement with the reference (DF-based liquid phase) both for stratiform and convective precipitations. The Ku-only-based products are in better agreement with DF-based products than Ka-only based ones. This is true for the precipitation phase as well as for the NSL or BB bottom identification. The results do not differ when the SF- and the DF-based both measured and derived integral DSD parameters (i.e., Z and R , respectively) are compared at NLS, with Ku-only estimates clearly outperforming Ka-only estimates. The microphysical DSD parameters show poor agreement between DF- and both SF-based products in terms of N_w , while it is slightly better in terms of D_m . In addition, the statistical scores (i.e., MD, RMSD, and FSD), calculated to quantify the difference between SF- and DF-based algorithms, also highlight that the agreement is better for stratiform precipitation than for convective precipitation, while the results between land and sea are comparable. The trend of the scores with respect to the parameters of interest (i.e., Z , D_m , N_w , or R) shows evidence that at higher precipitation intensities the attenuation affecting more on Ka- than on Ku-band joined to the different attenuation correction applied in the SF-based algorithms, the differences with the increase of DF-based. This is more evident for the Ka-band. Our results point out that at midlatitudes the discrepancies between the SF- and DF-based products depend mainly on radar frequency and to a lesser extent on precipitation and surface types. This leads to consider the estimation of the SF-based (especially Ka-only) DSD parameters less accurate when compared to the DF-based ones. Our results show that a user should take into account which DPR algorithm produced the estimate, since the accuracy has significant variability. Furthermore, the present results could be considered guideline for the DPR algorithm development team to improve the SF-based algorithm to reduce the discrepancies evidenced between SF- and DF-based products, at least at midlatitudes.

Starting from this analysis, the second part of the chapter focused on the validation of both microphysical and integral DSD parameters as estimated by DF-based DPR and combined DPR–GMI products, through the comparison with respect to GR estimates over Italy for 42 selected case studies. Although the GRs and the DPR work at different frequencies, C- and Ka-/Ku-band, respectively, the comparison of the reflectivity (limited to the comparison between C and Ku reflectivity) shows good agreement especially for stratiform precipitation over sea. Generally, both DPR and DPR–GMI products tend to overestimate D_m and N_w with a better performance during stratiform than convective precipitation for both parameters. While Ms and NS are equivalent for stratiform precipitation for both DPR and DPR–GMI products, during convective precipitation Ms outperforms NS. It has to be highlighted that both satellite- and ground-based N_w estimates fall in a very limited range of values reflecting what were found by Gatlin et al. (2020), which highlight the need to broaden the N_w a priori database to improve its estimation. The results for D_m are in quite good agreement with the findings of Gatlin et al. (2020), which validated the microphysical DSD parameters over the GPM VN while showing more marked differences for N_w . It is worth noting that both the working frequency of GRs used in this and in their study (C-band vs mainly S-band, respectively) and the procedure used to estimate the DSD parameters (empirical relationships vs NN approach, respectively) can play a role in obtaining different results. In addition, the GPM VN ingests data from a high number of GRs located at different geographical regions of the globe and covering a variety of meteorological regimes, while we limited our analysis to the Mediterranean area. Because of the slight (marked) overestimation of D_m (N_w), when an integral DSD parameter, as the rainfall rate, is estimated it results in an overestimation as well with respect to the reference values. The overestimation is marked especially for light precipitation, while the agreement improves moving from moderate to heavy rain rate. A sensitivity analysis did not show a deterioration of the results with respect to the distance of the matching point from the GR, neither on the presence of NUBF, while the sensitivity of the GR has to be carefully taken into account in the selection of the reference.

The results found for R , are similar to what found by Petracca et al. (2018), while they are generally opposite to the finding of Speirs et al. (2017) or Watters et al. (2018). This evidences that validation studies in different areas of the globe are necessary to have a fully comprehensive evaluation of GPM products as well as to quantify their dependence on location, terrain complexity, climate regime, etc. It has to be remarked also that the use of different release of the GPM algorithms (the present study and the above-cited works use different versions of the GPM algorithm) in the validation studies can play a crucial role in having similar or different results. A useful exercise could be to repeat a validation study on the same VN by using different releases of DPR (or generally of satellite-based) algorithms to quantify the impact of the changes on the satellite-based algorithm.

REFERENCES

- Adirosi, E., Baldini, L., Lombardo, F., Russo, F., Napolitano, F., Volpi, E., Tokay, A., 2015. Comparison of different fittings of drop spectra for rainfall retrievals. *Advances in Water Resources* 83, 55–67. <https://doi.org/10.1016/j.advwatres.2015.05.009>.
- Aires, F., Chédin, A., Scott, N.A., Rossow, W.B., 2002. A regularized neural net approach for retrieval of atmospheric and surface temperatures with the IASI instrument. *Journal of Applied Meteorology* 41 (2), 144–159. [https://doi.org/10.1175/1520-0450\(2002\)041<0144:ARNNAF>2.0.CO;2](https://doi.org/10.1175/1520-0450(2002)041<0144:ARNNAF>2.0.CO;2).
- Andsager, K., Beard, K.V., Laird, N.F., 1999. Laboratory measurements of axis ratios for large raindrops. *Journal of the Atmospheric Sciences* 56 (15), 2673–2683. [https://doi.org/10.1175/1520-0469\(1999\)056<2673:LMOARF>2.0.CO;2](https://doi.org/10.1175/1520-0469(1999)056<2673:LMOARF>2.0.CO;2).
- Battaglia, A., Tanelli, S., Heymsfield, G.M., Tian, L., 2014. The dual wavelength ratio Knee: A signature of multiple scattering in airborne Ku-Ka observations. *Journal of Applied Meteorology and Climatology* 53 (7), 1790–1808. <https://doi.org/10.1175/JAMC-D-13-0341.1>.
- Beard, K.V., Chuang, C., 1987. A new model for the equilibrium shape of raindrops. *Journal of the Atmospheric Sciences* 44 (11), 1509–1524. [https://doi.org/10.1175/1520-0469\(1987\)044<1509:anmfte>2.0.co;2](https://doi.org/10.1175/1520-0469(1987)044<1509:anmfte>2.0.co;2).
- Bech, J., Codina, B., Lorente, J., Bebbington, D., 2003. The sensitivity of single polarization weather radar beam blockage correction to variability in the vertical refractivity gradient. *Journal of Atmospheric and Oceanic Technology* 20 (6), 845–855. [https://doi.org/10.1175/1520-0426\(2003\)020<0845:TSOSPW>2.0.CO;2](https://doi.org/10.1175/1520-0426(2003)020<0845:TSOSPW>2.0.CO;2).
- Brandes, E.E., Zhang, G., Vivekanandan, J., 2002. Experiments in rainfall estimation with a polarimetric radar in a subtropical environment. *Journal of Applied Meteorology* 41 (6), 674–683. [https://doi.org/10.1175/1520-0450\(2002\)041<0674:EIREWA>2.0.CO;2](https://doi.org/10.1175/1520-0450(2002)041<0674:EIREWA>2.0.CO;2).
- Bringi, V.N., Chandrasekar, V., Balakrishnan, N., Zrnic, D.S., 1990. An examination of propagation effects in rainfall on radar measurements at microwave frequencies. *Journal of Atmospheric and Oceanic Technology* 7, 829–840. [https://doi.org/10.1175/1520-0426\(1990\)007,0829:AEOPFI.2.0.CO;2](https://doi.org/10.1175/1520-0426(1990)007,0829:AEOPFI.2.0.CO;2).
- Cao, Q., Zhang, G., Brandes, E.A., Schuur, T.J., 2010. Polarimetric radar rain estimation through retrieval of drop size distribution using a Bayesian approach. *Journal of Applied Meteorology and Climatology* 49 (5), 973–990. <https://doi.org/10.1175/2009JAMC2227.1>.
- Cao, Q., Zhang, G., Xue, M., 2013. A variational approach for retrieving raindrop size distribution from polarimetric radar measurements in the presence of attenuation. *Journal of Applied Meteorology and Climatology* 52 (1), 169–185. <https://doi.org/10.1175/JAMC-D-12-0101.1>.
- Caracciolo, C., Porcù, F., Prodi, F., 2008. Precipitation classification at mid-latitudes in terms of drop size distribution parameters. *Advances in Geosciences* 16, 11–17. <https://doi.org/10.5194/adgeo-16-11-2008>.
- Casella, D., Panegrossi, G., Sanò, P., Marra, A.C., Dietrich, S., Johnson, B.T., Kulie, M.S., 2017. Evaluation of the GPM-DPR snowfall detection capability: Comparison with CloudSat-CPR. *Atmospheric Research* 197, 64–75. <https://doi.org/10.1016/j.atmosres.2017.06.018>.
- Chandrasekar, V., Beauchamp, R. M., Chen, H., Vega, M., Schwaller, M., Petersen, W., & Wolff, D. (2015). Deployment and performance of NASA D3R during GPM IPHEX field campaign. In *International geoscience and remote sensing symposium (IGARSS)* (Vols.

- 2015-, pp. 2622–2625). Institute of Electrical and Electronics Engineers Inc. <https://doi.org/10.1109/IGARSS.2015.7326350>.
- Chen, H., & Chandrasekar, V. (2017). Characterization and estimation of precipitation over the Olympic mountains experiment (OLYMPEX) region. In *International geoscience and remote sensing symposium (IGARSS)* (Vols. 2017-, pp. 4538–4541). Institute of Electrical and Electronics Engineers Inc. <https://doi.org/10.1109/IGARSS.2017.8128011>
- Drobinski, P., Ducrocq, V., Alpert, P., Anagnostou, E., Béranger, K., Borga, M., Braud, I., Chanzy, A., Davolio, S., Delrieu, G., Estournel, C., Filali Boubrahmi, N., Font, J., Grubišić, V., Gualdi, S., Homar, V., Ivančan-Picek, B., Kottmeier, C., Kotroni, V., Wernli, H., 2014. HYMEX: A 10-year multidisciplinary program on the Mediterranean water cycle. *Bulletin of the American Meteorological Society* 95 (7), 1063–1082. <https://doi.org/10.1175/BAMS-D-12-00242.1>.
- D’Adderio, L.P., Porcù, F., Tokay, A., 2015. Identification and analysis of collisional breakup in natural rain. *Journal of the Atmospheric Sciences* 72 (9), 3404–3416. <https://doi.org/10.1175/JAS-D-14-0304.1>.
- D’Adderio, L.P., Vulpiani, G., Porcù, F., Tokay, A., Meneghini, R., 2018. Comparison of GPM core observatory and ground-based radar retrieval of mass-weighted mean raindrop diameter at midlatitude. *Journal of Hydrometeorology* 19 (10), 1583–1598. <https://doi.org/10.1175/JHM-D-18-0002.1>.
- Gatlin, P.N., Petersen, W.A., Pippitt, J.L., Berendes, T.A., Wolff, D.B., Tokay, A., 2020. The GPM validation network and evaluation of satellite-based retrievals of the rain drop size distribution. *Atmosphere* 11 (9). <https://doi.org/10.3390/atmos11091010>.
- Giorgi, F., 2006. Climate change hot-spots. *Geophysical Research Letters* 33 (8). <https://doi.org/10.1029/2006GL025734>.
- GPM File Spec NASA/JAXA. (2020). *Precipitation processing system global precipitation measurement: File specification for GPM products*. <http://ftp://gpmweb2.pps.eosdis.nasa.gov/pub/GPMfilespec/filespec.GPM.pdf>
- Grecu, M., Olson, W.S., Munchak, S.J., Ringerud, S., Liao, L., Haddad, Z., Kelley, B.L., McLaughlin, S.F., 2016. The GPM combined algorithm. *Journal of Atmospheric and Oceanic Technology* 33 (10), 2225–2245. <https://doi.org/10.1175/JTECH-D-16-0019.1>.
- Gunn, R., Kinzer, D.G., 1949. The terminal velocity of fall for water droplets in stagnant air. *Journal of Meteorology* 6 (4), 243–248. [https://doi.org/10.1175/1520-0469\(1949\)006<0243:ttvoff>2.0.co;2](https://doi.org/10.1175/1520-0469(1949)006<0243:ttvoff>2.0.co;2).
- Hamada, A., Takayabu, Y.N., 2016. Improvements in detection of light precipitation with the Global Precipitation Measurement dual-frequency precipitation radar (GPM DPR). *Journal of Atmospheric and Oceanic Technology* 33 (4), 653–667. <https://doi.org/10.1175/JTECH-D-15-0097.1>.
- Hou, A.Y., Kakar, R.K., Neeck, S., Azarbarzin, A.A., Kummerow, C.D., Kojima, M., Oki, R., Nakamura, K., Iguchi, T., 2014. The global precipitation measurement mission. *Bulletin of the American Meteorological Society* 95 (5), 701–722. <https://doi.org/10.1175/BAMS-D-13-00164.1>.
- Houze, R.A., McMurdie, L.A., Petersen, W.A., Schwall Er, M.R., Baccus, W., Lundquist, J.D., Mass, C.F., Nijssen, B., Rutledge, S.A., Hudak, D.R., Tanelli, S., Mace, G.G., Poellot, M.R., Lettenmaier, D.P., Zagrodnik, J.P., Rowe, A.K., DeHart, J.C., Madaus, L.E., Barnes, H.C., 2017. The Olympic mountains experiment (Olympex). *Bulletin of the American Meteorological Society* 98 (10), 2167–2188. <https://doi.org/10.1175/BAMS-D-16-0182.1>.

- Iguchi, T., Kawamoto, N., Oki, R., 2018. Detection of intense ice precipitation with GPM/DPR. *Journal of Atmospheric and Oceanic Technology* 35 (3), 491–502. <https://doi.org/10.1175/JTECH-D-17-0120.1>.
- Iguchi, Toshio. (2017). *NASA/JAXA. GPM/DPR level-2 algorithm theoretical basis document*. https://pmm.nasa.gov/sites/default/files/document_files/ATBD_DPR_201708_whole_1.pdf
- Kruger, A., Krajewski, W.F., 2002. Two-dimensional video disdrometer: A description. *Journal of Atmospheric and Oceanic Technology* 19 (5), 602–617. [https://doi.org/10.1175/1520-0426\(2002\)019<0602:TDVDAD>2.0.CO;2](https://doi.org/10.1175/1520-0426(2002)019<0602:TDVDAD>2.0.CO;2).
- Kubota, T., Iguchi, T., Kojima, M., Liao, L., Masaki, T., Hanado, H., Meneghini, R., Oki, R., 2016. A statistical method for reducing sidelobe clutter for the Ku-band precipitation radar on board the GPM core observatory. *Journal of Atmospheric and Oceanic Technology* 33 (7), 1413–1428. <https://doi.org/10.1175/JTECH-D-15-0202.1>.
- Lee, G.W., Zawadzki, I., 2005. Variability of drop size distributions: Noise and noise filtering in disdrometric data. *Journal of Applied Meteorology* 44 (5), 634–652. <https://doi.org/10.1175/JAM2222.1>.
- Marra, A.C., Federico, S., Montopoli, M., Avolio, E., Baldini, L., Casella, D., Adderio, L.P., Dietrich, S., Sanò, P., Torcasio, R.C., Panegrossi, G., 2019. The precipitation structure of the Mediterranean tropical-like Cyclone Numa: Analysis of GPM observations and numerical weather prediction model simulations. *Remote Sensing* 11 (14). <https://doi.org/10.3390/rs11141690>.
- Marra, A.C., Porcù, F., Baldini, L., Petracca, M., Casella, D., Dietrich, S., Mugnai, A., Sanò, P., Vulpiani, G., Panegrossi, G., 2017. Observational analysis of an exceptionally intense hailstorm over the Mediterranean area: Role of the GPM core observatory. *Atmospheric Research* 192, 72–90. <https://doi.org/10.1016/j.atmosres.2017.03.019>.
- Meneghini, R., Kim, H., Liao, L., Jones, J.A., Kwiatkowski, J.M., 2015. An initial assessment of the surface reference technique applied to data from the dual-frequency precipitation radar (DPR) on the GPM satellite. *Journal of Atmospheric and Oceanic Technology* 32 (12), 2281–2296. <https://doi.org/10.1175/JTECH-D-15-0044.1>.
- Mishchenko, M.I., 2000. Calculation of the amplitude matrix for a nonspherical particle in a fixed orientation. *Applied Optics* 39 (6), 1026–1031. <https://doi.org/10.1364/AO.39.001026>.
- Mroz, K., Battaglia, A., Lang, T.J., Cecil, D.J., Tanelli, S., Tridon, F., 2017. Hail-detection algorithm for the GPM core observatory satellite sensors. *Journal of Applied Meteorology and Climatology* 56 (7), 1939–1957. <https://doi.org/10.1175/JAMC-D-16-0368.1>.
- Ni, X., Liu, C., Cecil, D.J., Zhang, Q., 2017. On the detection of hail using satellite passive microwave radiometers and precipitation radar. *Journal of Applied Meteorology and Climatology* 56 (10), 2693–2709. <https://doi.org/10.1175/JAMC-D-17-0065.1>.
- Nurmi, P., 2003. Recommendations on the verification of local weather forecasts. Operation Department Finning Meteorological Institute, Technical Report
- Panegrossi, G., Casella, D., Dietrich, S., Marra, A.C., Sano, P., Mugnai, A., Baldini, L., Roberto, N., Adirosi, E., Cremonini, R., Bechini, R., Vulpiani, G., Petracca, M., Porcu, F., 2016. Use of the GPM constellation for monitoring heavy precipitation events over the Mediterranean Region. *IEEE Journal of Selected Topics in Applied Earth Observations and Remote Sensing* 9 (6), 2733–2753. <https://doi.org/10.1109/JSTARS.2016.2520660>.
- Panegrossi, G., Marra, A. C., Sanò, P., Baldini, L., Casella, D., & Porcù, F. (2020). Heavy precipitation systems in the Mediterranean area: The role of GPM. In *Advances in global*

- change research* (Vol. 69, pp. 819–841). Springer. https://doi.org/10.1007/978-3-030-35798-6_18.
- Petersen, W. A., Kirstetter, P. E., Wang, J., Wolff, D. B., & Tokay, A. (2020). The GPM ground validation program. In *Satellite precipitation measurements* (Vol. 69, pp. 471–502). Springer. https://doi.org/10.1007/978-3-030-35798-6_2.
- Petracca, M., D’Adderio, L.P., Porcù, F., Vulpiani, G., Sebastianelli, S., Puca, S., 2018. Validation of GPM dual-frequency precipitation radar (DPR) rainfall products over Italy. *Journal of Hydrometeorology* 19 (5), 907–925. <https://doi.org/10.1175/JHM-D-17-0144.1>.
- Schwaller, M.R., Robert Morris, K., 2011. A ground validation network for the global precipitation measurement mission. *Journal of Atmospheric and Oceanic Technology* 28 (3), 301–319. <https://doi.org/10.1175/2010JTECHA1403.1>.
- Seto, S., Shimozuma, T., Iguchi, T., & Kozu, T. (2016). Spatial and temporal variations of mass-weighted mean diameter estimated by GPM/DPR. In *International geoscience and remote sensing symposium (IGARSS)* (Vols. 2016-, pp. 3938–3940). Institute of Electrical and Electronics Engineers Inc. <https://doi.org/10.1109/IGARSS.2016.7730023>.
- Skofronick-Jackson, G., Petersen, W.A., Berg, W., Kidd, C., Stocker, E.F., Kirschbaum, D.B., Kakar, R., Braun, S.A., Huffman, G.J., Iguchi, T., Kirstetter, P.E., Kummerow, C., Meneghini, R., Oki, R., Olson, W.S., Takayabu, Y.N., Furukawa, K., Wilheit, T., 2017. The global precipitation measurement (GPM) mission for science and society. *Bulletin of the American Meteorological Society* 98 (8), 1679–1695. <https://doi.org/10.1175/BAMS-D-15-00306.1>.
- Somot, S., Taupier-Letage, I., Tintor, J., Uijlenhoet, R., Wernli, H., Richard, E., Romero, R., Rotunno, R., Roussot, O., Ruin, I., 2014. HYMEX: A 10-year multidisciplinary program on the Mediterranean water cycle. *Bulletin of the American Meteorological Society* 95 (7), 1063–1082. <https://doi.org/10.1175/BAMS-D-12-00242.1>.
- Speirs, P., Gabella, M., Berne, A., 2017. A comparison between the GPM dual-frequency precipitation radar and ground-based radar precipitation rate estimates in the Swiss Alps and Plateau. *Journal of Hydrometeorology* 18 (5), 1247–1269. <https://doi.org/10.1175/JHM-D-16-0085.1>.
- Tabary, P., 2007. The New French operational radar rainfall product. Part I: Methodology. *Weather and Forecasting* 22 (3), 393–408. <https://doi.org/10.1175/WAF1004.1>.
- Tanelli, S., Mace, G.G., Poellot, M.R., Lettenmaier, D.P., Zagrodnik, J.P., Rowe, A.K., DeHart, J.C., Madaus, L.E., Barnes, H.C., Hudak, D.R., 2017. The Olympic mountains experiment (Olympex). *Bulletin of the American Meteorological Society* 98 (10), 2167–2188. <https://doi.org/10.1175/BAMS-D-16-0182.1>.
- Thurai, M., Bringi, V.N., 2005. Drop axis ratios from a 2D video disdrometer. *Journal of Atmospheric and Oceanic Technology* 22 (7), 966–978. <https://doi.org/10.1175/JTECH1767.1>.
- Thurai, M., Bringi, V.N., Petersen, W.A., Gatlin, P.N., 2013. Drop shapes and fall speeds in rain: Two contrasting examples. *Journal of Applied Meteorology and Climatology* 52 (11), 2567–2581. <https://doi.org/10.1175/JAMC-D-12-085.1>.
- Thurai, M., Huang, G.J., Bringi, V.N., Randeu, W.L., Schönhuber, M., 2007. Drop shapes, model comparisons, and calculations of polarimetric radar parameters in rain. *Journal of Atmospheric and Oceanic Technology* 24 (6), 1019–1032. <https://doi.org/10.1175/JTECH2051.1>.
- Tokay, A., D’Adderio, L.P., Marks, D.A., Pippitt, J.L., Wolff, D.B., Petersen, W.A., 2020. Comparison of raindrop size distribution between NASA’s s-band polarimetric radar and

- two-dimensional video disdrometers. *Journal of Applied Meteorology and Climatology* 59 (3), 517–533. <https://doi.org/10.1175/JAMC-D-18-0339.1>.
- Tokay, A., D’Adderio, L.P., Wolff, D.B., Petersen, W.A., 2016. A field study of pixel-scale variability of raindrop size distribution in the Mid-Atlantic region. *Journal of Hydrometeorology* 17 (6), 1855–1868. <https://doi.org/10.1175/JHM-D-15-0159.1>.
- Tokay, Ali, D’Adderio, L.P., Porcù, F., Wolff, D.B., Petersen, W.A., 2017. A field study of footprint-scale variability of raindrop size distribution. *Journal of Hydrometeorology* 18, 3165–3179. <https://doi.org/10.1175/JHM-D-17-0003.1>.
- Vulpiani, G., Baldini, L., Roberto, N., 2015. Characterization of Mediterranean hail-bearing storms using an operational polarimetric X-band radar. *Atmospheric Measurement Techniques* 8 (11), 4681–4698. <https://doi.org/10.5194/amt-8-4681-2015>.
- Vulpiani, G., Marzano, F.S., Chandrasekar, V., Berne, A., Uijlenhoet, R., 2006. Polarimetric weather radar retrieval of raindrop size distribution by means of a regularized artificial neural network. *IEEE Transactions on Geoscience and Remote Sensing* 44, 3262–3275. <https://doi.org/10.1109/TGRS.2006.878438>.
- Vulpiani, G., Montopoli, M., Passeri, L.D., Gioia, A.G., Giordano, P., Marzano, F.S., 2012. On the use of dual-polarized C-band radar for operational rainfall retrieval in mountainous areas. *Journal of Applied Meteorology and Climatology* 51 (2), 405–425. <https://doi.org/10.1175/JAMC-D-10-05024.1>.
- Watters, D., Battaglia, A., Mroz, K., Tridon, F., 2018. Validation of the GPM version-5 surface rainfall products over Great Britain and Ireland. *Journal of Hydrometeorology* 19 (10), 1617–1636. <https://doi.org/10.1175/JHM-D-18-0051.1>.

FURTHER READING

- Tokay, A., Petersen, W.A., Gatlin, P., Wingo, M., 2013. Comparison of raindrop size distribution measurements by collocated disdrometers. *Journal of Atmospheric and Oceanic Technology* 30 (8), 1672–1690. <https://doi.org/10.1175/JTECH-D-12-00163.1>.
- Tokay, A., Wolff, D.B., Petersen, W.A., 2014. Evaluation of the new version of the laser-optical disdrometer, OTT parsivel. *Journal of Atmospheric and Oceanic Technology* 31 (6), 1276–1288. <https://doi.org/10.1175/JTECH-D-13-00174.1>.